Lithos 320–321 (2018) 378–402

Contents lists available at ScienceDirect

Lithos

journal homepage: www.elsevier.com/locate/lithos

Intermediate-depth brecciation along the subduction plate interface (Monviso eclogite, W. Alps)

Michele Locatelli [a,*], A. Verlaguet [a], P. Agard [a], L. Federico [b], S. Angiboust [c]

[a] Institut des Sciences de la Terre de Paris (ISTeP), Sorbonne Université, France
[b] Dipartimento di Scienze della Terra, dell'Ambiente e della Vita (DISTAV), Università di Genova, Italy
[c] Institut de Physique du Globe de Paris, Sorbonne Paris Cité, Univ. Paris Diderot, CNRS, F-75005 Paris, France

ARTICLE INFO

Article history:
Received 16 June 2018
Accepted 23 September 2018
Available online 28 September 2018

Keywords:
Eclogite-facies breccia
Plate interface
Monviso
Western Alps

ABSTRACT

The Monviso meta-ophiolite complex (Northern Italy, Western Alps) represents an almost intact fragment of Tethyan oceanic lithosphere metamorphosed at ~80 km depth (~2.6GPa–550 °C) during the Alpine subduction. We focus our study on a major shear zone cutting across this slab fragment at low angle (the Lower Shear Zone; LSZ). Here, in its talc and tremolite-rich serpentinite matrix, are embedded (together with metasedimentary lenses) variously brecciated Fe-Ti and Mg-Al metagabbro blocks. The latter were either interpreted as eclogitic breccias resulting from intermediate-depth rupture or as inherited, overprinted oceanic core complex features. Our new field, structural and petrographic data testify the genesis of this metagabbro breccia blocks at eclogite-facies conditions. Three types of eclogitic blocks can be distinguished, with non-random distribution (and decreasing size from top to base) throughout the ~200-m-thick and ~15 km-long LSZ: (1) Fe-Ti-metagabbros, brecciated and scattered in the upper to intermediate levels of the LSZ; (2) meter-size blocks and decameter-scale slivers of intact Mg-Al metagabbros, locally brecciated; (3) dm- to m-scale blocks of intact Fe-Ti metagabbros without breccia fabrics. Brecciation at eclogite facies conditions (at ~80 km depth) is documented by: i) the eclogitic foliation of intact Mg-Al-rich metagabbros (composed of omphacite + clinozoisite ± rutile and locally garnet) cut by breccia planes (cemented by omphacite + garnet ± lawsonite) and ii) the occurrence in breccia clasts of minerals that are fractured and offset along peak P-T omphacite-bearing planes. Rupture preferentially affected the Fe-Ti metagabbros, suggesting that rheological contrasts controlled the locus of brecciation. The occurrence of a first omphacite-rich matrix (M1, ~2.7GPa - 580 °C) crosscut by omphacite + garnet-bearing matrix M2 (~2.4GPa - 560 °C), witnesses multiple brittle rupture events, prior to a stage of eclogite facies fluid ingression marked by massive lawsonite recrystallization (matrix M3).
© 2018 Elsevier B.V. All rights reserved.

1. Introduction

Documenting processes acting at the subduction plate interface is fundamental for understanding (and modelling) interplate mechanical coupling, fluid migration pathways and/or processes triggering seismicity. Most field studies, geophysical investigations and mechanical models have focused on processes acting within the seismogenic zone (15–30 km-depth, Toyoshima, 1990), where megathrusts nucleate (Bachmann et al., 2009; Ikesawa et al., 2003; Meneghini et al., 2010; Rowe et al., 2005; Vannucchi et al., 2012). By contrast, there is a general lack of data on the mechanical and geochemical processes acting deeper (> ~40 km).

Two distinct seismic layers are recognized beyond the seismogenic zone (Fig. 1; Green and Houston, 1995; Hacker et al., 2003a, 2003b; Yamasaki and Seno, 2003); of these, geophysical and petrological data suggest that the upper one may correlate with the topmost, previously hydrothermalized crustal part of the slab ongoing massive metamorphic dehydration (Fig. 1; Bostock et al., 2002; Green and Houston, 1995; Hacker et al., 2003b; Rondenay et al., 2008). However, rheological processes associated with intermediate-depth seismicity (relocated between 40 and 300 km-depth; e.g., Nakajima et al., 2009; Preston et al., 2003; Shiina et al., 2013; Tsuji et al., 2008) and/or deep fluid circulation (e.g., hydraulic fracturing, dehydration embrittlement, mineral transformation induced faulting and pseudotachylites nucleation; Austrheim and Boundy, 1994; Davies, 1999; Hacker et al., 2003b; Jung and Green, 2004) are still largely debated due both to the lack of direct observations and to instrumental uncertainties (Kuge et al., 2010).

Although still limited, there is growing evidence that large-scale, “fossil” exhumed portions of subducted lithosphere (Agard et al., 2009), may record both chemical and mechanical processes operating in the depth range of intermediate-depth seismicity (e.g., Angiboust et al., 2011; Angiboust et al., 2012b; John et al., 2009; Kirby et al., 1996; Scambelluri et al., 2017; Yang et al., 2014). The recent report of

* Corresponding author.
E-mail address: locatellimichel@me.com (M. Locatelli).

https://doi.org/10.1016/j.lithos.2018.09.028
0024-4937/© 2018 Elsevier B.V. All rights reserved.

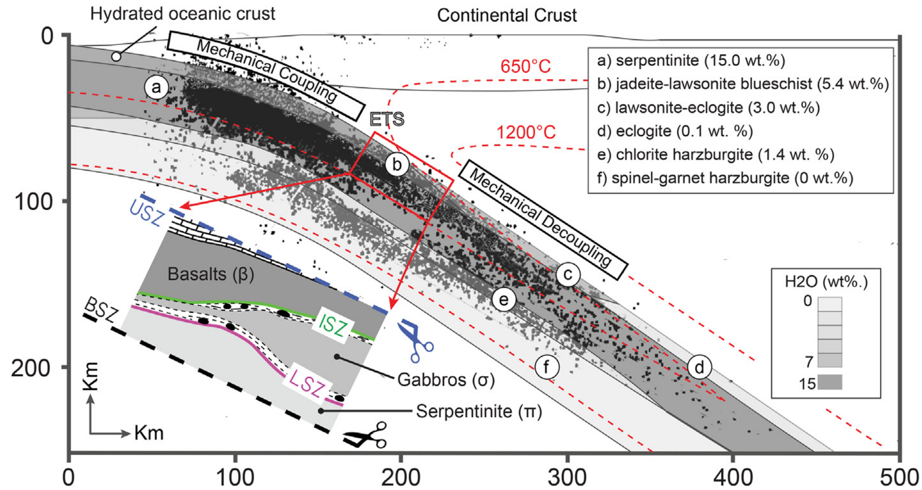

Fig. 1. Correlation between seismicity and mineral phase transformations in subduction zones (sketch refers to the Tohoku subduction zone, modified after Hacker et al., 2003a, 2003b). In the inset, the position of the Lago Superiore Unit (LSU) and its shear zones respect to the inferred P-T condition (This study and previous works: Schwartz et al., 2000; Groppo and Castelli, 2010; Angiboust et al., 2012a). In the box, the estimated water content (wt%). Isotherms from Peacock and Wang, 1999.

oceanic crust brecciation at eclogite facies conditions (in the Lago Superiore Unit of the Monviso meta-ophiolite, Western Alps; Angiboust et al., 2012a; Fig. 2) points to the possibility of retrieving patterns of intermediate-depth seismic rupture from a well-preserved slab fragment (Fig. 1). However, from structural and stratigraphic evidence, other authors interpreted these breccias as inherited pre-Alpine detachment fault rocks from an oceanic core complex or sedimentary-derived breccias (e.g., Balestro et al., 2018, Balestro et al., 2015a, 2015b; Festa et al., 2015). Furthermore, pre-subduction and pre-collision breccias are widely described in the Alpine ophiolites from the Central Alps (e.g., Desmurs et al., 2001), Western Alps (e.g., Manatschal and Müntener, 2009) and Corsica (Marroni and Pandolfi, 2007). Considerable debate also exists in the literature on the feasibility of brittle rock-failure at eclogite-facies conditions (e.g., Jin et al., 2001; Jung et al., 2004; Kirby et al., 1996; Raleigh, 1967; Raleigh and Paterson, 1965), leaving open the debate about their nature and origin.

The aims of this paper are therefore: i) to present evidence for eclogite-facies brecciation recorded by the metagabbro blocks disseminated in the Monviso shear zones (particularly in the Lower Shear Zone; LSZ); ii) to define their spatial extent and distribution across the LSZ; iii) to unravel the relative chronology of brecciation and associated mechanical/chemical changes and iv) to discuss their implications on intermediate-depth processes.

2. Geological setting

2.1. Regional geological setting

The Western Alps formed as a result of the eastward subduction of a branch of the Tethyan Ocean and of part of the thinned European continental margin beneath Adria, followed by collision from the Oligocene onwards (Coward and Dietrich, 1989; Lagabrielle and Lemoine, 1997; Laubscher, 1991; Schmid and Kissling, 2000). The reader is referred to more comprehensive publications for further details on the alpine geodynamic evolution (e.g., Agard et al., 2009; Beltrando et al., 2010).

The study area belongs to the ~30 km long Monviso meta-ophiolite complex (Fig. 2)*, one of the largest slices of oceanic lithosphere among the Liguro-Piemontese domain, which extends from the Voltri complex (Ligurian Alps, Italy) to the Zermatt-Saas zone (Valais, Switzerland and Valle D'Aosta, Italy).* Noteworthily, the structural and metamorphic

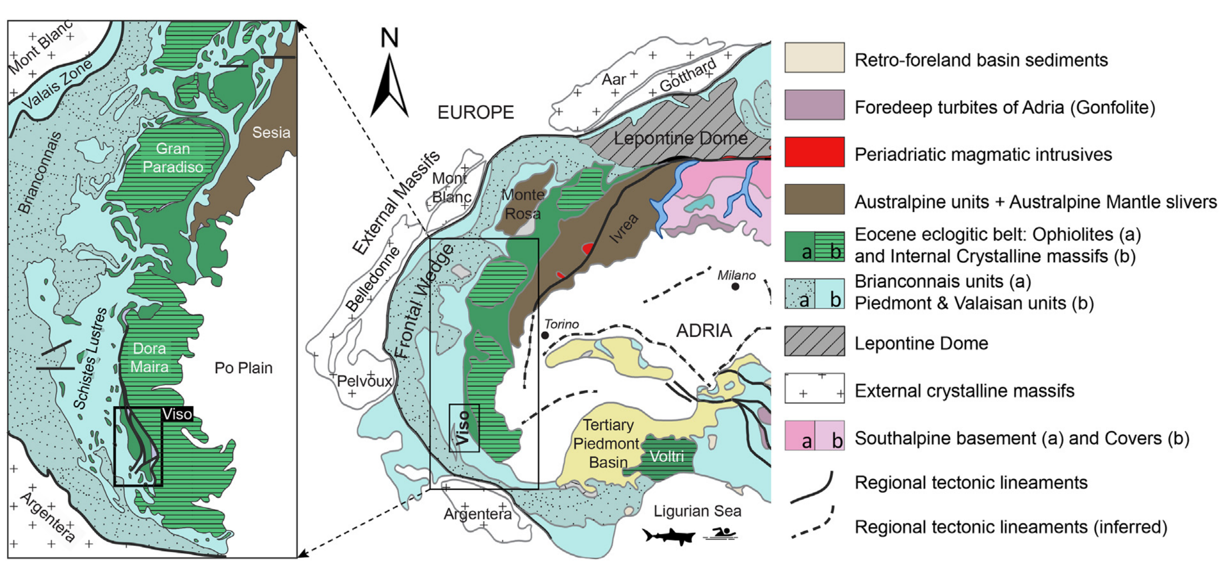

Fig. 2. Tectonic sketch of the Western Alps. The Eocene eclogitic belt (green) is exposed on the upper-plate side of the orogen, between the Frontal wedge (light blue) and the remnants of a Late Cretaceous doubly-vergent wedge (pink). In the inset, a detail of the eclogite belt and the frontal wedge with the localization of the Monviso metaophiolite. Maps modified after Malusà et al. (2011) and Agard et al. (2009).

characteristics of the Monviso are broadly comparable to those observed in the Zermatt-Saas and Voltri meta-ophiolites (e.g., Angiboust and Agard, 2010; Dal Piaz et al., 2003; Scambelluri et al., 1991; Schmid et al., 2004),

The Liguro-Piemontese domain is formed by the juxtaposition of km to 10 km-long exhumed eclogite-facies tectonic slices to lower grade (blueschist to eclogite facies) fragments of a fossil accretionary wedge, known as the Schistes Lustrés (e.g., Agard et al., 2002; Agard et al., 2009; Marthaler and Stampfli, 1989; Plunder et al., 2013).

A major westward-dipping normal shear zone system separates the Schistes Lustrés complex from the Monviso meta-ophiolite below (Fig. 2), exhibiting a metamorphic gap between the two units (respectively equilibrated at upper blueschist-facies and eclogite-facies peak conditions; e.g., Ballevre et al., 1990; Philippot, 1990). Below and to the east of the Monviso meta-ophiolite, separated by a ductile normal fault system (Blake and Jayko, 1990), the coesite-bearing Dora Maira massif represents a sliver of the thinned continental European distal margin involved in the Alpine subduction and detached from the downgoing slab during the Late Eocene.

Age constraints indicate that peak burial for the Monviso meta-ophiolite was achieved around 45–46 Ma (Duchêne et al., 1997; Rubatto and Angiboust, 2015; Rubatto and Hermann, 2003), while younger ages are inferred for the metamorphic peak of the Dora Maira massif (~120 km at 39–33 Ma; Castelli et al., 2007; Chopin, 2003, Chopin, 1984; Gebauer et al., 1997; Schertl et al., 1991).

2.2. Structure and P-T conditions of the Monviso meta-ophiolite

The Monviso meta-ophiolite provides well-preserved fragments of Tethyan oceanic lithosphere, with recognizable lithostratigraphic successions. It used to be subdivided into several tectonometamorphic units (Lombardo, 1978) and more recently in two main units: the Monviso s.s. unit (MU) and the Lago Superiore Unit (LSU; Angiboust et al., 2011). For the *Monviso Unit,* peak conditions of 480 °C/22 kbar were proposed by Angiboust et al. (2012a), whereas slightly different eclogitic peak temperatures were calculated for the *Lago Superiore Unit*: 580 °C (and 19 kbar; Schwartz et al., 2000), 650 °C (and 26 kbar; Messiga et al., 1999), 545 °C (and 20 kbar Castelli et al., 2002), 550 °C (and 25 kbar; Groppo and Castelli, 2010) and 550 °C (and 26 kbar; Angiboust et al., 2012a).

This study focuses on the LSU, which comprises, from bottom to top: serpentinized lherzolitic mantle intruded or capped by late Jurassic Mg-Al and/or Fe-Ti gabbros (152 Ma; Lombardo et al., 2002; 163 Ma, Rubatto and Hermann, 2003); banded tholeiitic basalts (with locally preserved pillow structures); diabases and mixed calcareous/pelitic Cretaceous metasediments (Balestro et al., 2013; Balestro et al., 2014; Castelli et al., 2002; Lombardo, 1978). Strong lateral variations in lithostratigraphy, with one or more of the above horizons missing, were attributed to an irregular seafloor structure typical of slow spreading oceans (Lagabrielle and Lemoine, 1997).

The original stratigraphic sequence is partly disrupted by shear zones (Angiboust et al., 2011; Angiboust et al., 2012a; Festa et al., 2015; Lombardo, 1978; Philippot and Kienast, 1989). We particularly focus on two of them (Figs. 3a, b and SM1): the Lower Shear Zone (LSZ) and the Intermediate Shear Zone (ISZ), which locally mark the metagabbros-serpentinites and metabasalts-metagabbros boundaries, respectively.

2.3. Intra-slab shear zones within the Lago Superiore unit: the Lower and Intermediate shear zones (LSZ, ISZ)

Two main km-scale shear zones partially disrupt the LSU unit of the Monviso meta-ophiolite, both made of a serpentinite-rich matrix embedding several kinds of blocks. The LSZ separates the main Mg-Al metagabbro body (to the west) from the underlying massive serpentinite sole constituting the eastern cliff of the meta-ophiolite Monviso massif (Figs. 3, 4a and SM1). In the study area, the shear zone has an extension along strike of over 15 km from the south (Colle di Luca pass) to the north (Rocce Fons) with a variable thickness ranging from ~300 m at Colle di Luca pass or Lago Superiore area to ~500 m at Pian Radice (Figs. 3a and SM1). The LSZ matrix is made of strongly deformed mylonitic serpentinite with locally interbedded cm to dm-thick layers of strongly sheared talc-chlorite schists. Serpentinite mainly consists of fine-grained, strongly-deformed antigorite (+/− magnetite, talc, magnesite and secondary olivine), whereas talc- and chlorite-schists contain lawsonite pseudomorphs, clinozoisite, light-green amphibole, rutile, apatite and rare quartz. Foliation inside the LSZ generally dips 20° to 40° to the W and rotates to the W-SW in the area around Ghincia Pastour and Lago Superiore (SM1). The mylonites usually show internal chaotic geometries with dragged, disharmonic folds (particularly around blocks and slices) progressively turning into mylonitic shear bands near the shear zone boundaries. Blocks of eclogite-facies gabbros, eclogitic metasediments and massive serpentinite (the first type being the most abundant) are embedded in the talc and tremolite-rich serpentinite matrix of the LSZ.

The ISZ cuts across the topmost part of the gabbroic sequence and extends for over 4 km from the Lago Superiore area to the north flank of Viso Mozzo, where it connects to the LSZ and pinches-out under the cover of Quaternary glacier deposits (Figs. 3a and SM1). Its thickness varies between 1 and 10 m and contains much less serpentinite matrix than the LSZ. Fe-Ti metagabbros outcropping along the ISZ directly at the top of Mg-Al metagabbros (notably in the Lago Superiore area; Figs. 3a, b and SM1) underwent mylonitization during eclogite-facies deformation, leading to the formation of a characteristic planar fabric dominated by an omphacitic clinopyroxene, garnet and rutile assemblage (Philippot and van Roermund, 1992). Eclogitic omphacite crack-seal veins, which occasionally crosscut these mylonitized gabbros, are believed to form by incremental opening associated with mylonitization (Philippot, 1987; Philippot and Kienast, 1989).

Structural characteristics, petrography and distribution of the blocks inside the LSZ (and partly the ISZ) are described and discussed in the next paragraphs.

3. Field mapping, sampling and methodology

To perform an exhaustive characterization of eclogite-facies blocks disseminated in the shear zones developed inside the LSU of Monviso meta-ophiolite, we adopted a “multi-scale” approach combining detailed fieldwork and meticulous structural and petrographic analysis of collected samples, as described below.

3.1. Field mapping of Monviso meta-ophiolites

A new geological map of the area was compiled (Map SM1, with 3D model in Fig. 3a), with a particularly detailed mapping of shear zones crosscutting the LSU (in particular the LSZ) and of the different block types disseminated inside. All field mapping was based on the 1:10.000-scale maps from the Regional Geographic Office of Piedmont (Italian CTR maps).

Four specific lithostratigraphic sequences analyzed along the strike of the LSU are presented in Fig. 3b to illustrate the important lithostratigraphic lateral variations inside the Monviso meta-ophiolite slice. Detailed logs and structural study were also performed on selected metasedimentary outcrops (West of Alpetto lake and Pra Fiorito Valley; SM2) in order to compare structures and compositions to those observed in mafic blocks.

3.2. Mapping of blocks: block nature and distribution

We describe as “blocks” all the solid, straight-sided bodies made of coherent rocks which appears to be still composed by their original lithology (e.g., non-metasomatized metagabbros, metasediments, etc.)

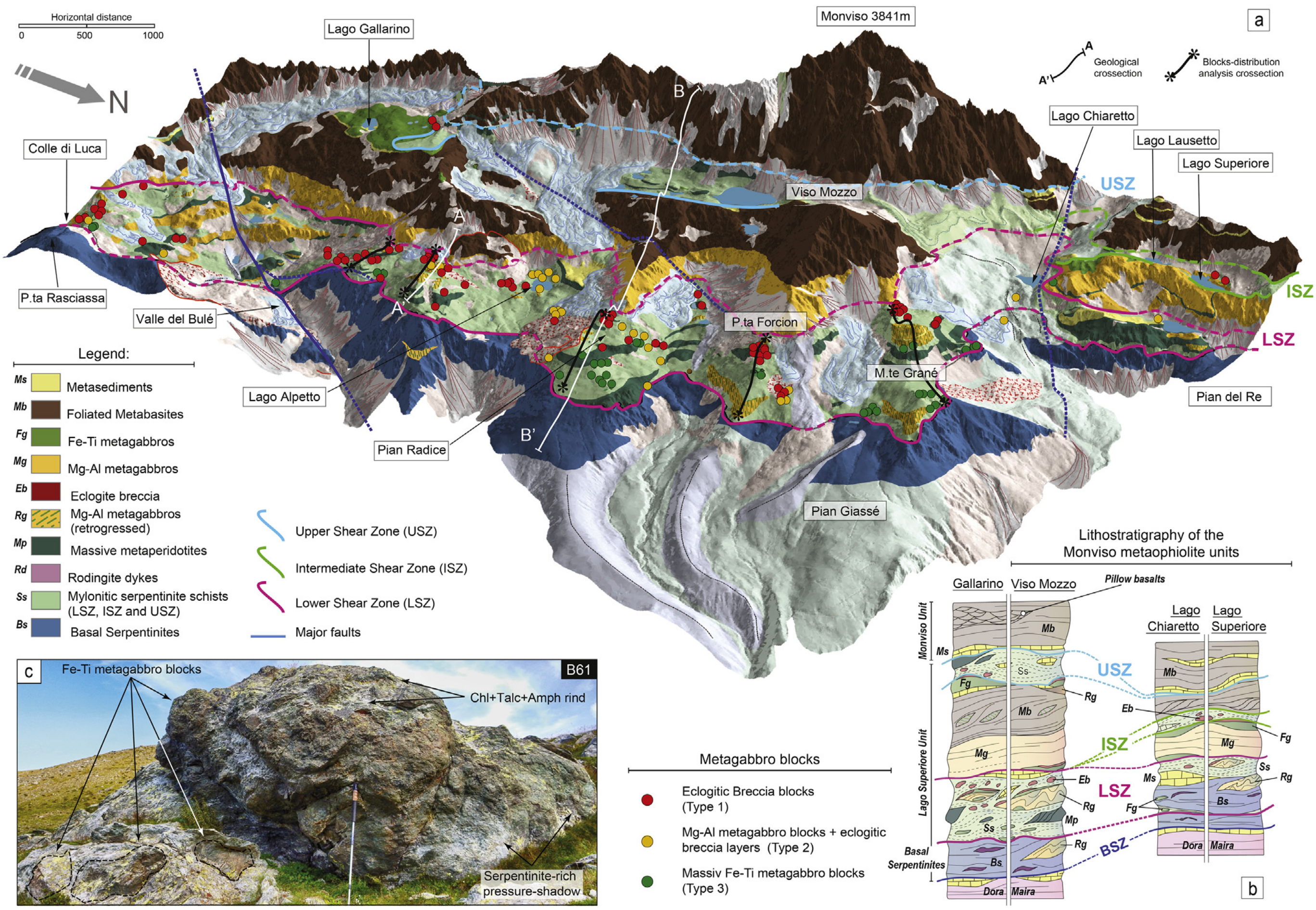

Fig. 3. (a) 3D rendering of the geology of the southern portion of the Monviso metaophiolite. White, full-lines represent the traces of the geological cross-section AA', BB'; black lines are the sections across the Lower shear zone (LSZ) where block distribution inside the shear zone was analyzed (more details in Fig. 5b). (b) Detailed stratigraphic logs across the Lago Superiore Unit (LSU) and the Monviso Unit (MU). From South to North the analyzed sectors are Gallarino, Viso Mozzo, Lago Chiaretto and Lago Superiore. For further details refer to the geological map presented in SM1. (c) Typical appearance of a m-scale metagabbro block from the LSZ. In evidence the pressure-shadows made by coherent (if compared to the bulk of the LSZ and ISZ) antigorite-rich schists with disseminated dm- to cm-scale clasts made by strongly-metasomatized metagabbros. Block B61, NE of Punta Murel.

and that are disseminated in the uncoherent mylonitic antigorite-schists composing the bulk of the LSZ and ISZ (Fig. 3c). A detailed field mapping of the different kinds of blocks, in particular Fe-Ti metagabbro blocks (more detail in section 5), was performed to determine their distribution and representativeness inside the LSZ (in particular) and ISZ. To overcome misinterpretation in block position due to erosional problems (i.e., blocks displaced by landslides; e.g., in the upper Bulé valley or north of Rocca del Lu; Fig. 3a and SM1), we used trigonometric calculations to re-locate the 3D position of blocks inside the LSZ across 5 preserved cross-sections (only for blocks whose position in the shear zone was preserved, as attested by intact primary contacts with the serpentinite foliation; Fig. 3a and SM1; see SM3 for details).

On SM4 are provided the detailed location, dimensions and structural characteristics of >180 blocks (for mapping, we considered a minimum block diameter of 1 m). Most of these are brecciated blocks, for which clast and matrix composition and relative proportions were also characterized.

3.3. Structural and image analysis of eclogitic brecciated blocks

A structural study at the outcrop scale was performed on brecciated blocks to characterize the rupture planes and was completed by image analysis run on ImageJ1.x software (Rueden et al., 2017) with dedicated windows distribution FiJi (Schindelin et al., 2012). On fresh eclogite-facies brecciated blocks, we measured (1) block length, width and height, (2) the clasts vs. matrix relative volumetric abundances, (3) the dimension and shape ratio of clasts, (4) the angle of misorientation between clast elongation axes or, where possible, between different clast foliations and (5) the number of clasts of different lithological composition.

Careful in-loco drawings and photographs were then analyzed using FiJi© image-analysis software (Schindelin et al., 2012) to retrieve clast areas, perimeters, angles of maximum elongation axis, aspect ratio and roundness. The last parameter was recalculated as adaption of the Waddel's sphericity, as suggested by Mort and Woodcock (2008). Automated clast detection was not feasible due to the poor color contrast between different clasts and matrices, so all clast contours were first manually outlined (paint software) and photographs converted to gray-scale images.

3.4. Microstructural and chemical analysis of clast and matrix: Analytical techniques

55 samples of brecciated blocks were drilled inside clasts, matrix, and at clast/matrix contacts for subsequent structural and chemical analysis. The microstructural study at the thin section scale was performed using both optical microscope and SEM (Zeiss Supra 55VP associated to SSD detector PTG Sahara for EDS analysis; ISTeP, UPMC). Mineral chemical compositions were then analyzed by EPMA (CAMECA FIVE and SX100) at CAMPARIS (UPMC, Paris), with analytical conditions for spot analysis of 15 kV, 10 nA, wavelength-dispersive spectroscopy (WDS) mode. Used standards were Fe_2O_3 (Fe), $MnTiO_3$ (Mn, Ti),

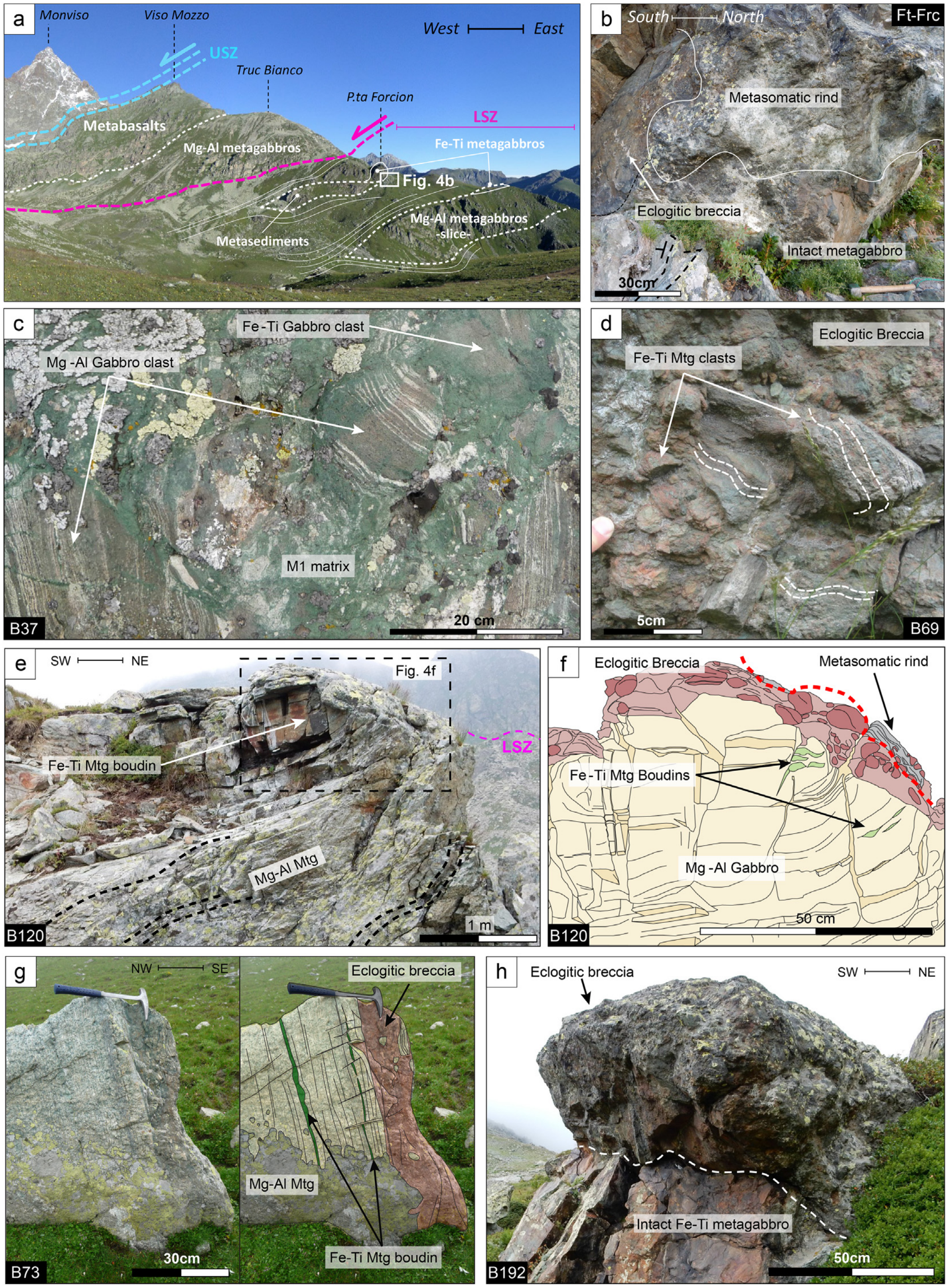

Fig. 4. (a) Panoramic view from Pian Radice to the North (Viso Mozzo). In evidence the stratigraphy of the Lago Superiore Unit with the position of the hanging wall of the Lower Shear Zone (LSZ; purple) and the Upper Shear Zone (USZ; blue). (For interpretation of the references to color in this figure legend, the reader is referred to the web version of this article.) (b) Detail of a Fe-Ti metagabbro outcrop at the base of the Mg-Al metagabbros constituting the *Truc Bianco* cliff. Notably, the intact Fe-Ti metagabbro is surrounded by a breccia layer with thickness up-to 50 cm, locally strongly metasomatized. Sampling location of specimen LSZ 63–15 (Fig.7d). (c) Typical clast-in-matrix appearance of eclogite-facies breccia on fresh surface. Here the rotated metagabbro clasts are cemented by omphacite-rich matrix (M1). Veins in the clasts are filled by fibrous omphacite ± apatite. Block B37, NW of Alpetto. (d) Typical appearance of eclogite breccia with strong weathering patina. The clast-in-matrix structure is still visible, with appreciable clasts rotation highlighted by foliation planes. Block B69, Punta Murel. (e-f) Example of a folded, mylonitic, eclogite-facies Mg-Al metagabbro unconformably cut by eclogite-facies breccia planes. Serpentinite-talcschists metasomatization is focused on the breccia matrix. Block B120, north of Punta Murel. (g) Typical m-scale Type2 block. The eclogitic breccia develops crosscutting (here at low angle) the pre-existing mylonitic foliation of the intact Mg-Al metagabbro. To be noted the Fe-Ti boudins in the intact metagabbro. Block B73, Prá Fiorito valley. (h) Transition from intact to brecciated rock recorded in a single Fe-Ti metagabbro block. Here the breccia thickness reach-up 80 cm. B192, south of Colle di Luca.

diopside (Mg, Si), CaF_2 (F), orthoclase (Al, K), anorthite (Ca) and albite (Na). In microprobe data, mineral FeO was assumed to be FeO-total, with Fe^{+3} recalculated based on stoichiometry and charge balance. Major elements bulk-rock compositions used for pseudosection modelling were analyzed by inductively coupled plasma-optical emission spectroscopy after fusion with LiBO3 and dissolution in HNO3. Li2O was analyzed by flame atomic absorption after fusion with Na2CO3 and dissolution in H3BO3. Fe2+ was analyzed by K2Cr2O7 titration after acid attack (HF–H2SO4). The H2O content was determined by loss on ignition.

4. Block types and distribution within shear zones

4.1. Eclogitic metagabbros in the LSZ

4.1.1. Block types

Two end-member lithologies make up the metagabbro blocks distributed in the LSZ: the Fe-Ti metagabbros, with the classical omphacite + garnet (+ rutile +/− pseudomorphs after lawsonite) paragenesis, and the lighter coloured Mg-Al metagabbros with (generally chromium-rich) omphacite, clinozoisite but no garnet. Mm- to cm-thick bands of garnet-bearing Mg-Al metagabbro are also present, mainly at the contact between Fe-Ti and Mg-Al metagabbros (e.g., around Fe-Ti-rich boudins or breccia layers).

Their morphology, structure and mineralogy allow to classify the blocks into three different groups:

(1) Type 1 blocks are made of completely brecciated metagabbros and are the most representative and spectacular of the eclogitic bodies dispersed in the LSZ (62% of mapped blocks, Min Vol. 0.05 m^3, Max Vol. 2613.81 m^3; see SM3, 4, 5). They present a peculiar clast-in-matrix structure (Fig. 4b, c, d), with clasts almost exclusively made of mylonitic Fe-Ti metagabbros with rare Mg-Al gabbros (~10%), cemented by an omphacite-rich matrix (+/− garnet and pseudomorphs after lawsonite). Matrix proportions vary, from block to block, from <10 vol% to up to >50 vol %. Dimension and extent of rotation of the clasts are also variable (for details, SM3, 4, 5).

(2) Type 2 blocks (22% of mapped blocks, Min Vol. 1.51 m^3, Max Vol. 125,663.71 m^3) are made of unbrecciated, foliated Mg-Al metagabbros showing strong internal mylonitization and complex folding. They locally embed up to 5 m thick unbrecciated boudins of Fe-Ti metagabbros (Fig. 4e, f, g). Although relatively rare (only 3% of the mapped blocks; see SM3, 4 and 5), there are some large hm-scale slivers of Type 2 blocks (Colle Di Luca: B196; Punta Murel: B169; Lago dell'Alpetto: B7; SM6). In both cases, Type 2 blocks foliation is in places abruptly truncated by planes of brecciated Type 1 Fe-Ti metagabbros (Fig. 4e, f, g, h). These Fe-Ti breccia planes always bound the hm-scale Type 2 blocks on their western flank (Fig. 5a, b; i.e., facing the Mg-Al metagabbro cliff, dipping 20° to 60° to the W; Fig. 3a, SM6a, b, c, d) and are absent on the other side.

At the outcrop-scale, the clast-in-matrix structure of eclogite breccias of Type 1 and Type 2 blocks is made of mylonitic clasts rotated to variable degrees and cemented by interstitial matrix (Fig. 4c, d), with structures comparable to those observed at the micro-scale (i.e., discordant mylonitic foliation underlined by rutile beds; see below).

(3) Type 3 blocks are characterized by finely-foliated to massive, unbrecciated Fe-Ti metagabbro blocks (16% of mapped blocks, Min Vol. 1.56 m^3, Max Vol. 6.00 m^3). Coarse grained fabrics are preserved in the core of the largest blocks (> 10 m^3, e.g., Pian Radice area) and consist in almost undeformed coronitic garnet (< 6 mm) crystallizing around megacrystals of omphacite (< 8 mm), which were interpreted as pseudomorphs after magmatic pyroxene or plagioclase (Angiboust et al., 2011; Groppo and Castelli, 2010; Lombardo, 1978; Philippot and van Roermund, 1992; Pognante and Kienast, 1987).

All blocks are coated by late, variably thick metasomatic rinds (Figs. 3c, 4b).

4.1.2. Metagabbro block distribution within the LSZ

Detailed mapping along the 15 km-long LSZ suggests a non-chaotic distribution of the metagabbro blocks (Fig. 5a and SM1): Type 1 and Type 2 blocks preferentially crop out in the intermediate-to-upper part of the shear zone, whereas unbrecciated Type 3 blocks are restricted to the lower part of the LSZ (Fig. 5b).

Block distribution in the shear zone also depends on the volume of the blocks (Fig. 5b): the largest Type 1 breccia blocks (~80% of mapped Type 1 blocks, average volume > 50 m^3) are restricted to the upper part of the shear zone, whereas smaller blocks (~20%, with average volume of 10 m^3) are spread in the lower part of the LSZ. Most Type 2 blocks (~76%) and all Type 1 blocks are located stratigraphically above the big slivers of retrogressed Mg-Al metagabbro of Punta Murel, Colle di Luca and Alpetto Lake (Type 2). Unbrecciated Type 3 blocks, which are restricted to a 30–100 m thick-band at the base of the LSZ, show a general volume increase towards the serpentinite sole, with eclogitic bodies reaching volumes of 20 m^3 SW of Monte Granè (Fig. 5b; more details in SM4).

4.2. Serpentinite, metasedimentary and jadeitite blocks in the LSZ

Several massive serpentinite blocks and slivers are disseminated in the lower portion of the shear zone (Fig. 3a, b and SM1), associated to rounded, unbrecciated Fe-Ti metagabbro blocks (Type 3 blocks) and rare meta-rodingite boudins.

Meter-scale lenses of metasediments are also dispersed within the LSZ, decreasing in abundance from N to S. Large slivers (up to 90 m thick) were only observed in Lago Superiore, Pra Fiorito and Alpetto area (Fig. 3a, b and SM1). Metasediments are calcschists and marbles metamorphosed under eclogite facies P-T conditions. Large slivers preserve evidence for alternations of metadolostones, quartz-mica-rich sandstones, garnet-lawsonite-chloritoid-paragonite-rich micaschists and meta-conglomerate strata. The latter, frequently clast-supported, are composed of mm to dm (< 50 cm) clasts of gabbro, basalt and peridotite mixed with a strongly deformed sedimentary matrix (Fig. SM2a, b). Clasts are well rounded and elongated (aspect ratio up to 4), often boudinaged (Fig. SM2c, d) and indicative of strong deformation (e.g., bodies West of Alpetto Lake or in the upper Pra Fiorito Valley). For example, the W-dipping metasedimentary sliver outcropping in the Pra Fiorito Valley (Fig. 3a and SM1a) shows three clast-supported and four matrix-supported fining-upward conglomerate layers (Fig. SM2e), with a progressive decrease of serpentinite and relative increase of (meta) basaltic clasts from base to top of the outcrop.

In the LSZ rare meter-size blocks of jadeitite are also found (especially in the upper Bulé valley and Colle di Luca; see Castelli et al. (2002) and Compagnoni et al. (2012) for details. Nevertheless, their origin is unclear: the lack of primary contacts with the shear zone mylonite and their uneven distribution in the LSZ may suggest quaternary erosion of the upper Mg-Al metagabbro cliff and the subsequent dissemination of this blocks in the LSZ.

4.3. Comparison with block types and distribution in the ISZ

Rare, m-scale Type 1 brecciated blocks crop out chiefly on the western and eastern side of Lago Superiore (Fig. 3a and SM1). Interestingly, these blocks stratigraphically overlay the Fe-Ti gabbro sills intruded in the eclogitic Mg-Al metagabbros outcropping south-east of the Lausetto Lake, following a stratigraphic scheme also observed in the USZ (Fig. 3b). Moreover, meter-scale metabasaltic blocks (hanging wall of the ISZ) are found in the ISZ together with scarce metasedimentary blocks. In the southern part of the shear zone, for example North-East of Chiaretto Lake (Fig. SM1), are scattered big slivers (up to 60 m long) of massive serpentinite and metasediments. The latter shows a strong deformation with N/S to NW/SE-trending major fold axis and W-verging fold limbs describing clockwise *Z*-shaped W-verging parasitic folds. The presence of allocthonous serpentinized metaperidotite and metasediment slivers in the ISZ suggests the disruption of the preexisting ophiolitic sequence along this shear zone (Fig. 3a, b and SM1).

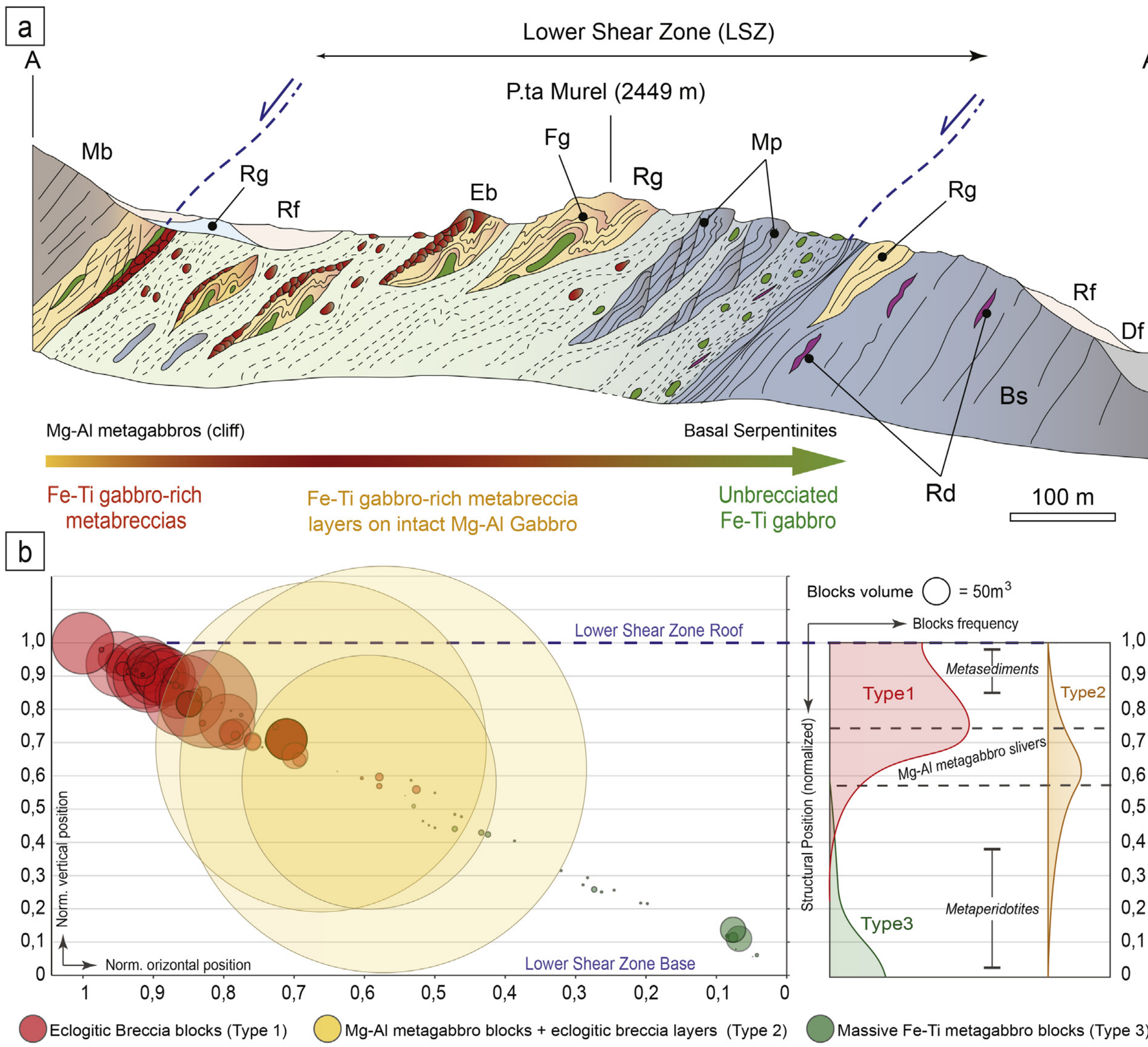

Fig. 5. (a) Geological cross-section across the Lower Shear Zone (Punta Murel area). We enlighted the ordered distribution (dip towards West) of the breccia planes in the detached Mg-Al metagabbros slices dispersed in the LSZ. Unbrecciated Fe-Ti metagabbro blocks are concentrated at the base of LSZ. *Mb*: metabasalts; *Rg*: inactive rock glacier; *Rf*: rock-fall deposits; *Eb*: eclogite breccias; *Fg*: Fe-Ti metagabbros; *Rg*: retrogressed Mg-Al metagabbros; *Mp*: massive peridotites (serpentinized); *Rd*: metarodingite dykes; *Bs*: basal serpentinites; *Df*: debris flow. (b) Diagram showing the distribution of metagabbro blocks inside the LSZ. The larger part of eclogite breccia blocks (Type 1) outcrops in the upper part of LSZ, above the Mg-Al metagabbro slices, with the unbrecciated Fe-Ti metagabbro blocks (Type 3) located at the base. On X-axis the normalized horizontal distance of blocks from the base of LSZ and on Y-axis the normalized vertical distance of blocks from the base of LSZ.

5. Brecciation patterns

5.1. Outcrop scale structural patterns

The structural study of breccia horizons was limited by the small size (80% < 5 m) of most blocks that do not preserve the full width of breccia planes and by the widespread talc + amphibole + chlorite-rich metasomatic coating that hinders the block surfaces. Nevertheless, several blocks from the LSZ exhibit the complete transition from intact metagabbros to completely brecciated horizons (Fig. 6a, b): five Type 2 blocks were chosen among them to conduct a detailed structural analysis (in Prà Fiorito valley, north of Alpetto Lake and in the upper Bulè Valley; Fig. SM1). Type 2 blocks usually present only one single brecciation horizon, more rarely multiple brecciation planes (Fig. 6c, SM6e, f), sharply truncating the preexisting eclogite-facies mylonitic foliation (Fig. 4e, f, g). >80% of analyzed clasts have an area smaller than 10 cm^2 and 90% of the clasts in breccia horizons are <30 cm^2, with power-law distribution (Fig. SM5c).

In complete breccia planes, the rim to core sequence is characterized by a strong decrease in clast size and increase in clast rotation angle, clast roundness and matrix vs clast amount (Fig. 6a). The progressive transition from intact rock to crackle, mosaic and finally chaotic-breccia zones in the Fe-Ti breccia planes (Fig. 6a, b) is similar to the classic rim-to-core sequence observed in tectonic breccias (Jébrak, 1997; Mort and Woodcock, 2008; Sibson, 1986):

(1) near the rupture surfaces, crackle breccia layers (10–30 cm thick) are characterized by very angular clasts (Fig. 6b) detached from the fault walls by a complex array of fractures (Fig. 6a, b), with limited displacement (≤ 2 cm) and almost no rotation. Eclogite clasts, locally with diameters up-to 40 cm, exhibit jigsaw texture (Sibson, 1986). Matrix represents only 10 vol%.

(2) textures progressively shift to mosaic breccia textures (20–50 cm thick, Fig. 6b), with a higher matrix content (< 45% of total volume, with up to 1 cm thick matrix layers; Fig. 6a, b), smaller clasts (< 20 cm) and slight clast rotation (< 10°).

(3) Breccia core portions (20–50 cm thick, “chaotic breccia s.l.”) are matrix supported (> 55% of total volume). The clasts are smaller (more that 80% of clast <5 cm^2), have aspect ratio < 2 and are randomly oriented (Fig. 6b), giving rise to chaotic breccia fabrics. The transition from crackle to chaotic breccia shows also a progressive increase in

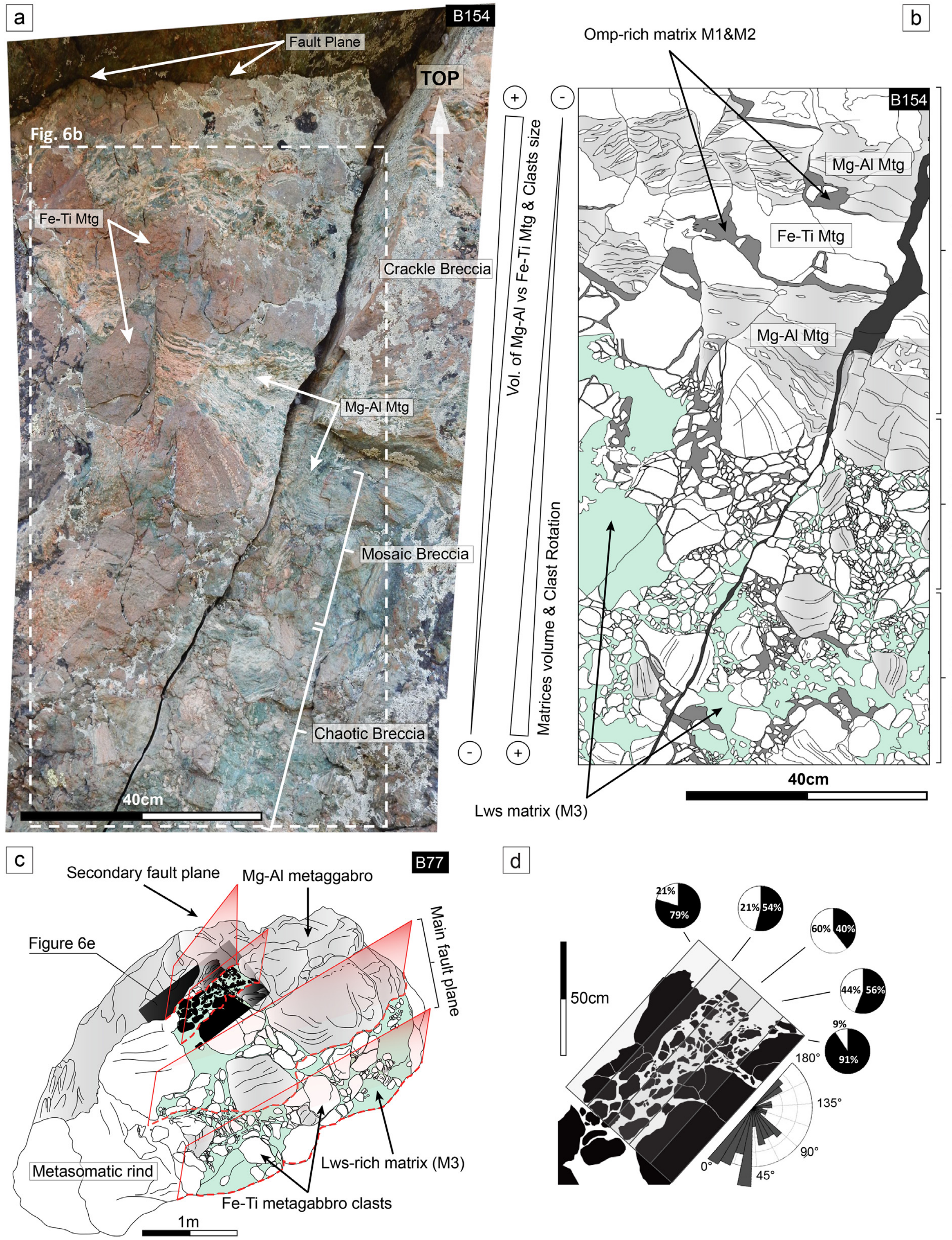

Fig. 6. (a) A fully preserved eclogite-breccia fault-plane. Breccia fabrics show the transition from crackle breccia (at the top) to chaotic breccia (at the core), according to the definitions of Mort and Woodcock (2008). Block B154, Pra Fiorito valley. (b) schematic drawing of the clast-in-matrix structures observed in preserved eclogite-facies breccia planes. Used color-code: Fe-Ti metagabbro clast (white), Mg-Al metagabbro clasts (light gray), Omphacite-rich matrix (dark gray), Lws-rich matrix (light green). Block B154, Pra Fiorito valley. (c) Sketch of an eclogite-facies breccia block characterized by multiple rupture surfaces. The black box locates Fig. 6e. Original photo of the block in supplementary material SM6e. Block B77, Pra Fiorito Valley. (d) Schematic sketch of the minor breccia plane in the block B77 with the evaluated volumetric percentage of clasts (black) vs matrix (white) on 5 equal-area sectors. In the inset, the orientation of the maximum elongation axis of the clasts dispersed in the matrix with respect to the single minor breccia plane. Only clasts with aspect ratio > 2 where analyzed.

the modal amount of Fe-Ti metagabbro clasts vs Mg-Al metagabbro clasts (Fig. 6a), the latter absent from breccia cores.

The analysis of the orientation of the maximum-elongation axis of the clasts with respect to the inferred rupture planes (Fig. 6d and, for comparison, SM6f) reveals that in each single breccia horizon, the clast orientations are not totally random: there are preferred orientations, particularly around 20° ± 10° and 40° ± 10° (Fig. 6d). On the contrary, taking into account all the breccia planes present in one block (when multiple, Fig. 6c), clast distribution is random, with angles ranging from 0° to 180° (Fig. SM7f).

In most cases, rotated clasts were cemented after brecciation by a newly-formed matrix. Textural and compositional characteristics of the clasts and the four successive matrix types observed are described below.

Note that in the ISZ, only 4 small brecciated metagabbro blocks were observed (Type1) and thus none of them record a full brecciation plane.

5.2. Different types of clast and matrix at the decimeter to millimeter scale

In brecciated eclogite-facies blocks (Type1), the clasts are constituted by Fe-Ti metagabbro (90% of modal amount) and rarer Mg-rich metagabbros (mostly close to the unbrecciated rock, 10% of modal amount). Mg-Al metagabbro clasts show the same fabrics and composition than Mg-Al metagabbros constituting the western cliff of the LSZ (Fig. 3a) and forming most of Type 2 blocks, whereas mylonitized Fe-Ti metagabbro clasts are comparable to the Fe-Ti metagabbro boudins embedded in Type 2 blocks. The mylonitic foliation of the Fe-Ti

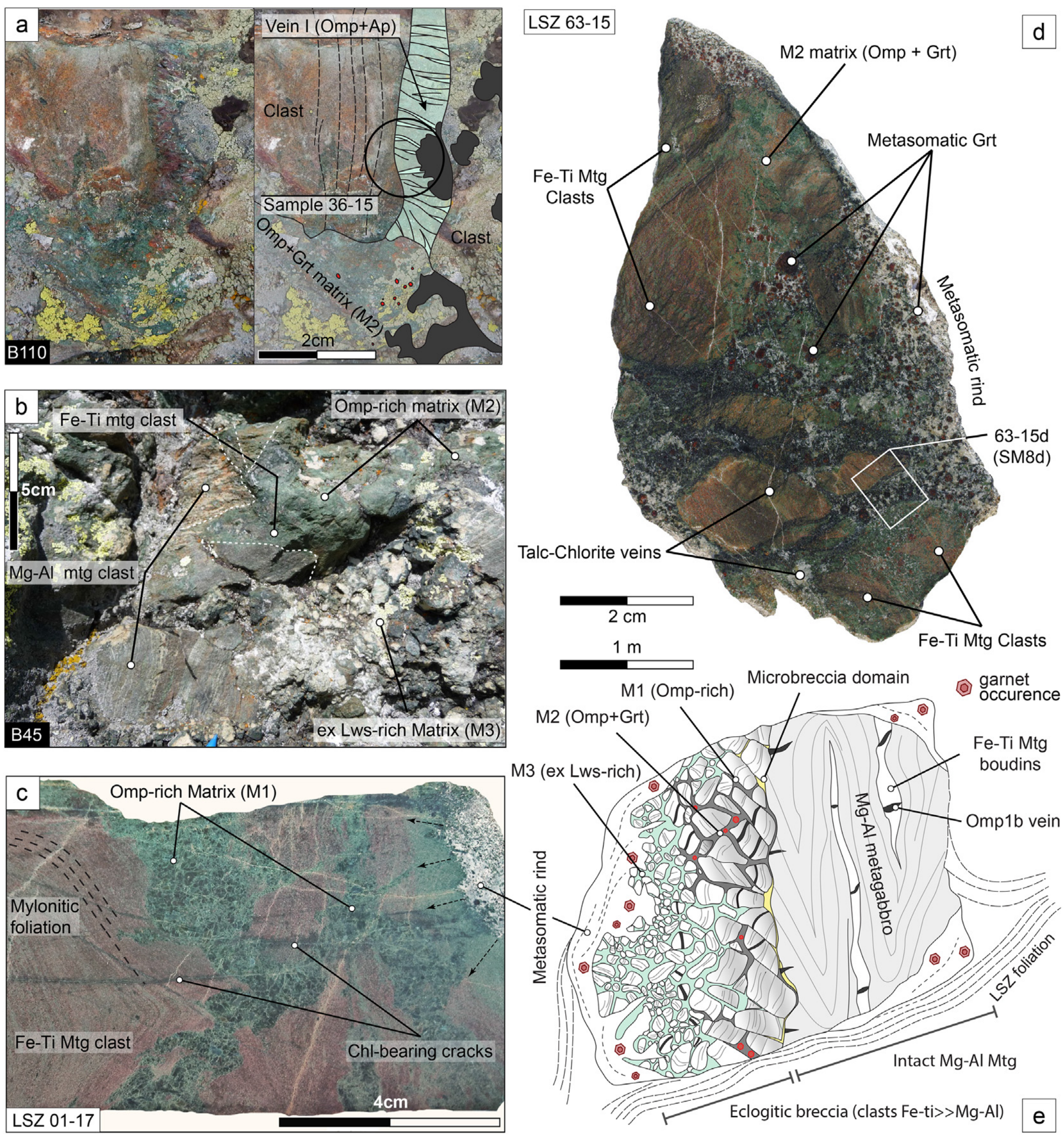

Fig. 7. Meso-structures of eclogite breccias. (a) Eclogitic vein with fibrous omphacite + apatite crystals developed in a mylonitic, eclogite-facies Fe-Ti metagabbro clast. Coarse-grain omphacite + garnet matrix (deep-green color) seals all the previous structures. Block B110, Intermediate Shear Zone (West of Lago Superiore). (For interpretation of the references to color in this figure legend, the reader is referred to the web version of this article.) (b) Eclogitic metagabbro clasts (evident the mylonitic foliations) sealed by (ex)lawsonite-rich matrix. Noteworthy, in the upper-center part of the picture, the occurrence of a clast composed by reworked eclogite-facies breccia (mylonitic metagabbro clasts cemented by omphacite-rich matrix M1). Block B45, South of Punta Murel. (c) Mylonitic, eclogite-facies fragments of finely-grained and folded Fe-Ti metagabbro sealed by omphacite-rich M1 matrix; in evidence the mm-scale, euhedral omphacite grains of M1 matrix. This sample clearly shows the development of the talc-, chlorite-, amphibole- and garnet-rich metasomatism (and associated selvages - dashed arrows-) affecting all the metagabbro breccias found in the ISZ and LSZ. Sample LSZ01–17, E of P.ta Forcion. (d) Polished sample of eclogite breccia evidencing the crosscutting relationship between mylonitic clasts, the omphacite + garnet matrix (M2) and the metasomatic rind mineralization (talc + chlorite + garnet + amphibole ± Ca-rich diopside). The darker areas (mainly developed in the matrix portions) are chlorite/amphibole-rich recrystallization linked to late-stage retrogression under green-schist condition. Sample LSZ 63–15, from the base of Truc Bianco cliff (Fig. 4b). (e) Schematic reconstruction of the structures developed in blocks with fully-preserved transition from intact rock to breccia layers. Such type of blocks corresponds to the “Type 2” described in the text (e.g. the big sliver of Punta Murel -B69- or the smaller blocks B154 in Pra Fiorito valley).

gabbro clasts is locally crosscut by omphacite-rich veins (Figs. 7a) up-to 1 cm wide, which locally include host-rock fragments. Opening geometries vary from crack-seal to tension gashes, similar to geometries of veins crosscutting the Lago-Superiore Fe-Ti metagabbros (Philippot, 1987; Spandler et al., 2011). Some of these veins are crosscut by the matrix sealing the clasts, and thus predate the brecciation event (Veins I; Fig. 7a), while others (Veins II, mainly observed in the ISZ) locally crosscut both clasts and the omphacite-rich matrix (or M1, hereafter), postdating the first brecciation event.

In these brecciated metagabbro blocks, clasts are partly sealed by a matrix whose amount increases from rims to cores of breccia levels (Figs. 4c, 6a, b); crosscutting and textural relationships allow distinguishing four successive matrix types (Fig. 7):

(1) At the transition between intact rock and crackle brecciated layers (Fig. 7e), slightly rotated clasts are surrounded by anastomosed, sub-millimetric domains (called "microbreccia" hereafter) made of omphacite and garnet grains showing strong grain-size reduction (< 100 μm) and re-orientation parallel to the clasts borders.

(2) Such domains are sealed by small amounts of a light green omphacitic cement (hereafter called M1, Figs. 4c and 7c), whose amount increases (up-to 1 cm-thick mantles around clasts; Figs. 6a, b) while the microbreccia progressively disappears from the inner to outer levels of crackle breccias.

(3) Along the crackle-mosaic breccia transition (Fig. 6a, b, c), M1 matrix progressively turns into another omphacite-matrix type (M2), which also contains garnet visible in hand-specimen (Fig. 7a).

(4) In the inner portion of brecciated layers (i.e., chaotic breccia fabrics), crosscutting relationships show that a late matrix M3 postdates both M1 and M2 (Figs. 6a, b, c, 7b). M3 is the most abundant matrix type (Fig. 7e) and is characterized by impressive euhedral lozenge-shape pseudomorphs after lawsonite (< 2 cm; Figs. 7b). Noteworthily, all these matrices lack any evidence of pervasive mylonitic deformation (e.g., Fig. 7c) and/or foliation.

At the contact with the antigorite-rich matrix embedding the blocks in the LSZ, blocks are rimmed by a hydrated metasomatic rind (composed by talc, chlorite, garnet, acicular amphibole, diopside and rare phengite) that can locally be up to 0.5 m-thick (e.g., in Lago Superiore, Pta. Forcion and Colle di Luca; Fig. 4b). This metasomatic replacement affects both clasts and matrix, and thus postdates brecciation. Matrix zones are more strongly affected, however, and a complex set of sub-millimeter scale veins filled with hydrous minerals nucleate in the retrogressed matrix and radially crosscut the surrounding clasts (e.g., Fig. 7a, b, c, d). The degree of metasomatism rapidly decreases from block rims to cores, clearly suggesting an external fluid-assisted metasomatic event postdating both brecciation and block dismembering in the LSZ.

Note that the scarce brecciated metagabbro blocks sampled in the ISZ show similar structures (i.e., clasts locally crosscut by veins and embedded in matrix) but only small amount M2 matrix (Fig. 7a). Indeed, no extensive M3 lawsonite-rich matrix was observed in the poorly developed brecciated layers of these rocks.

All the structural relationships between clasts and matrices described above are summarized in Fig. 7e.

6. Clast and matrix: mineralogy and microstructure

6.1. Clast mineralogy and microstructure

Fe-Ti metagabbro clasts are mainly composed of omphacite (up to 60 vol%) garnet (35 vol%), and rutile (Fig. 8a, b, c; Table 1). Euhedral omphacite and rutile crystals underline a well-developed mylonitic foliation. Here, rutile aggregates, grown at the expense of magmatic ilmenite, locally form polycrystalline ribbons up-to 70 μm-thick aligned along the mylonitic foliation (Fig. 8a). The dynamic recrystallization of omphacite results in grains with an aspect-ratio up to 1:15 elongated parallel to the foliation (Fig. 8b). Their irregular grain boundaries (both in the mylonitic foliation plane and in the pressure shadows, Fig. 8a, b) indicate grain-boundary migration processes during the ductile mylonitic deformation. Sub-idioblastic garnets (200–500 μm) show conspicuous zoning under the microscope, with rims poorer in omphacite and rutile inclusions with respect to the cores (Fig. 8a). In the latter, folded omphacite crystals and rutile trails (Fig. 8c) underline garnet *syn*-kinematic growth. Local occurrence of randomly distributed square or lozenge-shape patches filled with fine grained (< 20 μm size, SM7a) clinozoisite and white micas are interpreted as pseudomorphs after lawsonite crystals. Foliation planes folded around these aggregates suggest that lawsonite crystallization was pre- to syn-kinematic with respect to Fe-Ti metagabbro ductile deformation, and thus coeval with the P-T peak eclogitic paragenesis. Other accessory minerals are sub-idiomorphic apatite, randomly distributed acicular glaucophane crystals (< 1 vol% in these rocks), rare quartz (included in garnet cores) and small paragonite crystals (< 2 vol%, < 50 μm long) parallel to the main foliation (Table 1). Locally, sub-mm-sized deep-green porphyroclasts embedded in the foliation are interpreted as relic crystals of magmatic clinopyroxene completely re-equilibrated as omphacite. Similarly, mm-scale porphyroclasts associated to coronitic garnet and interstitial rutile (Fig. 8d) are observed in the rare, low-strained Type 3 blocks of Fe-Ti metagabbros found at the base of the LSZ (Figs. 3a, 5 and SM1). Here, contrary to the above described mylonitic clasts, omphacite porphyroclasts show only rare undulose extinction and kink bands (Fig. 8d), which attests to minor ductile deformation. Such rock fabric is thus interpreted as the result of the static, topotactic recrystallization of omphacite after clinopyroxene, garnet after plagioclase and rutile after titanite (or ilmenite) on the pre-existing magmatic texture of Fe-Ti rich gabbros (e.g., Messiga et al., 1999; Philippot and van Roermund, 1992).

The rare Mg-Al metagabbro clasts are made of mm-thick bands of deep-green omphacite alternating with whitish clinozoisite horizons (up to 1.5 cm; Fig. 4c). Glaucophane and pseudomorphs after lawsonite are occasionally found in the eclogitic foliation of these clasts (Table 1). Although garnet is absent in the Mg-richest lithologies, mm- to cm-thick garnet-rich layers are frequently observed inside gabbro layers showing a composition intermediate between Fe-Ti and Mg-Al metagabbros.

The mylonitic foliation of clasts is locally crosscut by mm- to cm-scale veins (Fig. 7a). They consist mainly of (i) acicular omphacite and secondary apatite crystals (Veins I), locally deflected at the contact with the clast host-rock (Figs. 8e) or (ii) tabular omphacite grains associated to mm-scale garnet and rutile (Veins II). Veins I formation is postdated by the crystallization of the matrix M1, while the crystallization of Veins II appear to be earlier to that of matrix M2 and M3, which seal all the structures developed in metagabbro blocks before the brecciation (e.g., Figs. 6a-b, 7a-c and 8f).

6.2. Matrix mineralogy and microstructure

Table 1 summarizes the mineralogy of the four successive matrix types wrapping the eclogitic Fe-Ti and Mg-Al clasts of brecciated metagabbros (Fig. 7e).

In rare cases, the absence of matrix between clasts in the levels of crackle breccia nearest to the intact rocks (Fig. 6b) results in micrometric garnet offset (Fig. 8g) and pressure-solution-like fabrics at sharp clast-clast contacts, with progressive deflection of clast mylonitic foliation, and strong grain-size reduction and reorientation of mylonitic omphacite.

In the outer part of breccia planes (i.e., at the contact with intact rock; Fig. 7e), clasts are separated by sub-millimetric microbreccia domains, composed of sharply-fractured crystals of omphacite, garnet, apatite and rutile, i.e., the mineral assemblage present in the surrounding clasts. There, garnet crystals are fragmented and rounded, whereas rutile and omphacite are crudely reoriented parallel to clast boundaries, with a strong grain size reduction for omphacite down to 10 μm

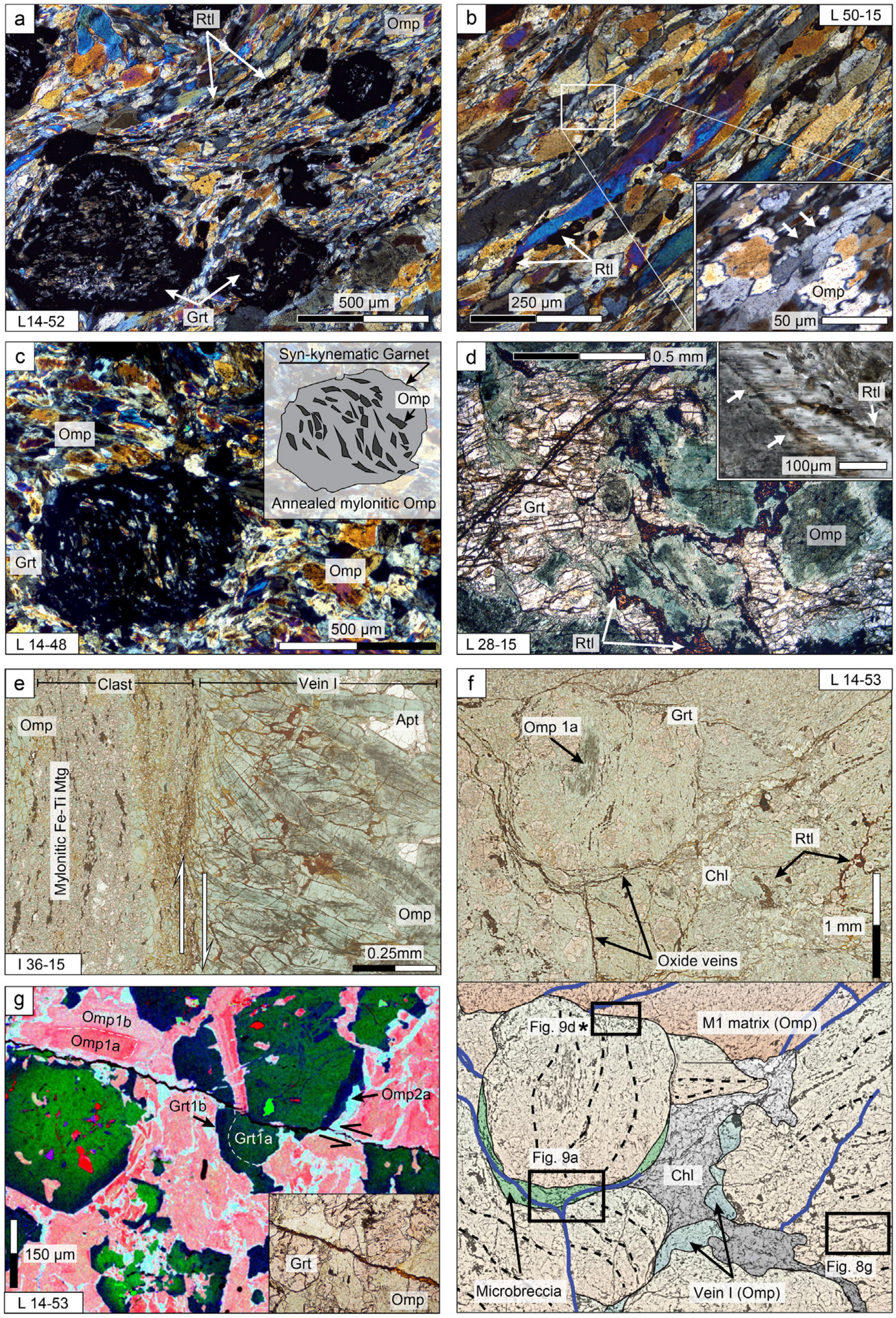

Fig. 8. Microstructures of eclogite breccias as seen under optical polarizing microscope, if not otherwise indicated. Pictures (d, e, f) plane polarized light; (a, b,c) cross polarized light. (a) Mylonitic, eclogite-facies foliation of a Fe-Ti metagabbro clasts with the omphacite-rich, rutile-free pressure shadows developed around mylonitic garnet porphyroblasts. In the latter the cores are extremely-rich in inclusions of omphacite ± glaucophane (sample L14–52, LSZ). (b) Detail of the mylonitic, eclogite-facies foliation of a Fe-Ti metagabbro clasts. Omphacite grains crystallize with an aspect-ratio up to 1:15, elongated parallel to the foliation. Their irregular grain boundaries (detail in the box) indicate that grain-boundary migration processes were active during ductile deformation. (sample L50–15, LSZ) (c) Syn-kinematic garnet, with preserved omphacite trails inclusions, growth in a mylonitic (partially annealed) Fe-Ti metagabbro clasts (sample L14–48, LSZ). (d) In rare, low-strained metagabbros blocks (type 3 blocks), evidences for topotactic replacement of the pre-existing magmatic fabric is preserved. Here mm-scale omphacite porphyroclasts (crystalizing after magmatic clinopyroxene) are associated to coronitic garnet (after plagioclase) and interstitial rutile (after titanite). In the box: a rare kink-band developed inside an omphacite porphyroclast, attesting minor ductile deformation. Sample L28–15, LSZ. (e) Photomicrograph of a sheared omphacite-rich vein grown inside a mylonitic Fe-Ti metagabbro clast. The top-to-the right sense of shear is derived by the deflection direction of the acicular omphacite megacrystals. Sample I36–15, ISZ. (f) Upper box: clast-in-matrix fabric developed at mm-scale in the crackle breccia horizon of sample L14–53 (LSZ). Clasts rotation and eclogite-facies matrix crystallization are evident and are totally comparable to those observed at the meso-scale. Lower-box: interpretation of the structures and mineralogy observed. To be noted (*): thin-section of Fig.9d is from the same rock sample but different thin-section (cut on the same microstructural location). (g) Micrometric garnet and omphacite offset along omphacite-bearing microfractures, evidencing an apparent displacement of ~250 µm. Color-code for the FEG-SEM quantified map: Ca (Green), Na (Red) and Mg (Blue). Sample L14–53, LSZ.

(by comparison: 200 µm in clasts) and progressive deflection of clast mylonitic foliation (Figs. 9a, b, c).

M1 matrix consists of almost pure deep green omphacite (euhedral crystals up to 200 µm-long; Fig. 7c), with few euhedral apatite crystals and subordinate lawsonite pseudomorphs and talc. Scarce sub-millimetric corroded rutile and pyrite overgrown by iron oxides are dispersed close to clast-matrix borders. Contacts between clasts and matrix are usually sharp (Fig. 7c and 8f), but FEG-SEM quantified

Table 1
Summary of eclogite-facies assemblages, their relative abundances and associated mineralogy in eclogitic breccia blocks.

		Omp	*Grt*	*Lws*	*Rt*	*Czo*	*Ap*	*Na-Amp*	*Ca-Di*	*Ph*	*Tlc*	*Chl*
Clasts	*Fe-Ti clast*	++	++	(rare)[a]	++		(rare)					
	(Mineralogy)	(Omp1a + Omp1b)	(Grt1a + Grt1b)									
	Mg-Al clast	++	(rare)	(rare)[a]	+	++	(rare)			(rare)		(rare)
	(Mineralogy)	(Omp1a + Omp1b)	(Grt1a + Grt1b)									
	Vein I	++			+[b]		+					
	(Mineralogy)	(Omp1b)										
	Vein II	++	(rare)							(rare)		
	(Mineralogy)	(Omp2b)	(Grt2b)									
Matrices	*Microbreccia*	++	++		+		+					
	(Mineralogy)	(Omp2a + Omp1a[b]/b[b])	(Grt2a overg. on Grt1)									
	M1	++										
	(Mineralogy)	(Omp2b > Omp2a-Omp1a[b]/b[b])										
	M2	++	+	+[a]						(rare)		
	(Mineralogy)	(Omp2b> > Omp2a-Omp1a[b]/b[b])	(Grt2b)									
	M3	+	+[a]	+[a]								
	(Mineralogy)	(Omp2b)	(Grt2?)									
	Metasom. Rinds		+				(rare)	+	+	+	++	+
	(Mineralogy)		(Grt3)									

Adopted abbrevations for rock-forming minerals are from Whitney and Evans (2010). *Omp*: omphacite, *Grt*: garnet, *Lws*: lawsonite, *Rt*: rutile, *Czo*: clinozoisite, *Ap*: apatite, *Na-Amp*: sodic amphibole, *Ca-Di*: calcic diopside, *Ph*: phengite, *Tlc*: talc, *Chl*: chlorite.
[a] Pseudomorphs after lawsonite (microcrystalline Czo, Ph and Chl) and garnet (Chl aggregates with bended rutile trails).
[b] Relict crystal fragments derived from clasts and dispersed in vein/matrix.

maps exhibit complex radial infiltration patterns of M1-like omphacite inside clasts (Fig. 9d). This fabric, characterized by clasts irregularly fractured and cemented by M1, is also well visible at the outcrop scale (Fig. 4c).

M2 matrix assemblage is omphacite-dominated too, but contains additional garnet and rare rutile and lawsonite pseudomorphs (for LSZ and ISZ; Fig. 9e). The tabular omphacite crystals are locally up-to 300 μm-long, with straight grain boundaries and common triple-points junctions (Fig. 9f). the The grains shows only minor undulose extinction (Fig. 9f), without development of any foliation. Euhedral garnet (Fig. 9e) is clearly less fractured than in mylonitic foliation of the clasts, but also shows zoning, with inclusion-rich cores (omphacite ± rutile) rimmed by inclusion-poor mantles. Accessory minerals are titanite and rare deep-blue acicular glaucophane, the latter crystallizing as interstitial phase between omphacite grains.

In breccia cores, matrix M3 is characterized by cm-sized euhedral lozenge-shape pseudomorphs after lawsonite (Figs. 7b and 9g). Lawsonite pseudomorphs are filled with a mesh of microcrystalline clinozoisite, paragonite and chlorite (up to 10 μm), which likely results from late epidote-blueschist facies retrogression. These lawsonite pseudomorphs are indeed surrounded by the following greenschist-facies assemblage: tremolite-actinolite (constituting >40% of M3 matrix) + chlorite + calcite + albite + epidote. However, textural arguments show that this greenschist assemblage replaced a former eclogite-facies paragenesis: occurrence of rare relicts of sub-mm omphacite inside tremolite-actinolite crystals, mm-thick tabular rutile in textural equilibrium with lawsonite crystals, and chlorite filling large (up to 0.2 mm) rounded domains with preserved rutile trails (Fig. SM7b, c) are suggestive of garnet pseudomorphs. Therefore, the mineralogy of the M3 matrix may have been very close to that of M2 (i.e., classical eclogitic paragenesis), but with a much higher proportion of lawsonite.

Contrary to the sharp contacts observed between clasts and M1 or M2 matrix, clasts contacts with M3 matrix are smoothed by the overgrowth of the greenschist-facies assemblage (Fig. 9g).

This late greenschist retrogression affected all matrix types, but was much more pervasive in M3, (M3 > M2 > M1), indicating that retrogression was limited in matrices with less hydrous phases (i.e., M1). External fluid ingression is nevertheless attested locally by late veins (Fig.7c) and interstitial domains (up-to 5 mm-thick) between clasts filled with greenschist fan-shaped chlorite aggregates (Fig. 8f). Fe-rich veins (up to 50 wt% FeO, thickness up-to 50 μm) nucleate in these domains and crosscut the samples, preferentially following the clast-clast or clast-matrix boundaries, again clearly postdating brecciation. In several blocks from LSZ, especially in Type 2, a complex array of fibrous glaucophane veins (thickness up-to 2 cm) crosscut both clasts and matrices, postdating the brecciation.

6.3. Metasomatic rinds

At their contact with the surrounding antigorite schist forming the matrix of LSZ, the mafic eclogitic breccias are strongly affected by a widespread metasomatism (Figs. 3c, 4b), which affects preferentially matrices (Figs. 7c and SM 7d). The pre-existing eclogite-facies assemblages are replaced by a mesh of talc and chlorite, a new-generation of brown metasomatic garnet, acicular amphibole and diopside plus very rare phengite. Lawsonite pseudomorphs (now replaced by epidote + paragonite) in textural equilibrium with the surrounding talc and metasomatic-stage chlorite are also observed, together with relicts of omphacite crystals and dispersed rutile. A complex set of sub-millimeter scale veins of syntaxial talc, diopside and chlorite radiates from the hydrated metasomatic domains into the clasts (Figs. 7c-d). Similarly to block matrices, metasomatic rinds were locally replaced by a later, cross-cutting greenschist facies assemblage (chlorite, tremolite-actinolite, calcite, rare quartz).

7. Mineral chemistry

Both clast and matrix mineral compositions are given in Tables 2 and 3.

7.1. Clast mineral chemistry

In the mylonitic Fe-Ti metagabbro clasts, the first generation of omphacite (Omp1a, $Di_{45}Jd_{30}Ae_{25}$; Fig. 10a, b) forms the bright cores of large, partially dismembered porphyroclasts. These are rimmed by a second omphacite generation (Omp1b, $Di_{40}Jd_{38}Ae_{22}$; Fig. 10a, b) crystallizing also as newly formed crystals aligned in the mylonitic foliation. Garnet is also zoned (Fig. 8a), with dark-pink coloured cores (Grt1a, $Grs_{24}Prp_5Alm_{71}$; Fig. 10c) and lighter rims (Grt1b, $Grs_{17}Prp_{13}Alm_{70}$; Fig. 10c); garnet cores are locally affected by complex radial fractures (Fig. SM8b) filled and sealed by Grt1b compositions. Smaller garnets (< 100 μm) with Grt1b composition are also scattered in the foliation. Interestingly, garnet cores (Grt1a) are full of Omp1a inclusions, whereas garnet rims (Grt1b) only contain few inclusions of

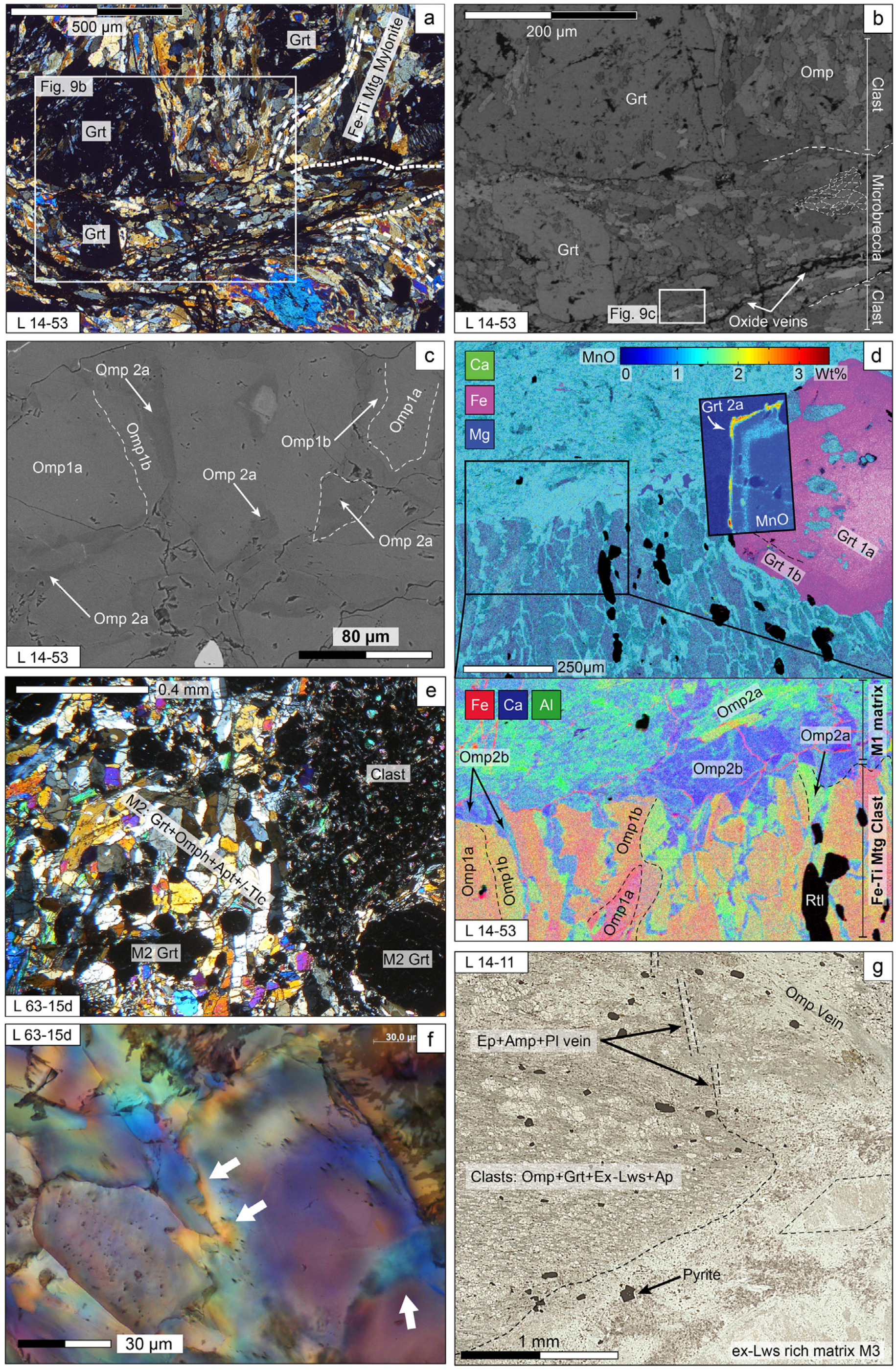

Fig. 9. Microstructures of eclogite breccias as seen under optical polarizing microscope, if not otherwise indicated. Picture (a, e, g) plane polarized light; (f) cross polarized light. (a) Microfractured omphacite, garnett and rutile crystals crudely re-oriented in the "microbreccia" domains locally preserved between clasts. Notably, garnet shapes are sharp-edged. Later-stage Fe-rich veins preferentially infiltrate in these domains. Sample L14–53, LSZ. (b) SEM image evidencing the strong grain-size reduction and the omphacite and rutile crystals re-orientation at the sharp transition between a mylonitic-clast and microbreccia domain. Sample L14–53, LSZ. (c) SEM image showing the complex zonation of omphacite crystals in the "microbreccia" domains, with mylonitic Omp1a and Omp1b sealed by a third generation of omphacite Omp2a. As observed for garnets, crystals have sharp-edged shapes. Quantified EPMA map of these domains are presented in Fig. SM8a. (d) FEG-SEM quantified maps of the transition between a mylonitic Fe-Ti metagabbro clast (at the bottom) and the omphacite-rich matrix M1 (at the top). In evidence the infiltration-like geometries of Omp2b inside the clast departing from M1. Color-scale in the figure. In the upper box: EPMA quantified map showing the MnO enrichment of garnet generation Grt2a. Sample L14–53, LSZ. (e) Photomicrograph of the big hypidiomorphic omphacite crystals and inclusion-poor garnets constituting the bulk of M2 matrix. Note the sharp contact clast-M2 matrix. Sample L63–15b, LSZ. (f) M2 matrix omphacite grains: detail photomicrograph of the tabular grain boundaries crystallizing at triple-points junctions (120°) and straight borders. Only here minor undulose extinction is observed, whereas no evidence for mylonitization is shown. Sample L63–15b, LSZ. (g) Photomicrograph of the transition between an Mg-Al metagabbro clast and ex-Lws rich matrix M3. The un-sharp contact between clast and matrix is linked to the massive green-schist recrystallization that partly obliterated the pre-existing structures. Sample L14–11, LSZ. See Fig. SM7a-b for more detail on matrix M3 paragenesis.

Omp1b, showing that omphacite and garnet compositions evolved jointly during mylonitization.

In the outer-most clast domains, a third generation of interstitial Al-rich omphacite (Omp2a, peak composition $Di_{46}Jd_{48}Ae_{6}$; Fig. 10a, b) crystallized as rims around the previous omphacite crystals with complex, asymmetric patterns (Fig. 9d). Interestingly, omphacite crystallizing in the pressure-solution planes promoting micrometric garnet offset (Fig. 8g) is in equilibrium with Omp2a (Fig. 10a, b). Finally,

Table 2
representative major elements analysis (wt%) of omphacite subdivided by microstructural domains.

	Omphacite included in Garnet					Mylonitic Fe-Ti clasts						Grt offset planes*	
Sample	L14-50	L14-53	L14-50	L14-53	L63-15	I31-15	I31-15	I31-15	I31-15	I31-15	I31-15	L14-53	L14-53
Generation	Omp1a (in Grt1a)	Omp1b (in Grt1b)	Omp1b (in Grt1b)	Omp1a (in Grt1a)	Omp2b (in Grt2a)	Omp1a	Omp1a	Omp1a	Omp1b	Omp1b	Omp1b	Omp2a	Omp2a
SiO_2	55,33	55,43	54,50	55,32	55,51	54,77	54,88	54,89	54,80	54,40	54,94	56,52	55,84
TiO_2	0,06	0,04	0,06	0,05	0,09	*0,10*	*0,05*	*0,07*	0,03	0,03	0,04	0,10	0,34
Al_2O_3	7,80	8,89	8,80	6,95	9,02	5,52	6,89	6,46	5,12	4,69	6,67	10,32	8,92
Cr_2O_3	0,06	0,04	0,04	0,03	0,02	0,08	0,00	0,08	0,05	0,06	0,07	0,08	0,06
FeO	11,02	11,33	10,46	10,18	9,62	10,09	10,92	11,61	7,30	8,51	7,79	5,90	7,14
MnO	0,01	0,04	0,03	0,07	0,08	0,00	0,03	0,02	0,13	0,00	0,06	0,04	0,10
MgO	6,34	5,66	6,07	7,78	6,20	8,40	7,14	6,90	10,44	9,74	9,03	8,17	7,88
CaO	10,14	9,01	9,88	12,10	9,83	12,96	11,12	10,97	16,24	15,49	14,16	11,09	12,49
Na_2O	8,45	9,07	8,74	7,44	8,66	6,81	7,77	7,69	5,19	5,47	6,33	7,72	7,09
Total	99,2	99,5	98,6	99,9	99,0	98,5	98,8	98,7	99,3	98,4	99,1	99,9	99,9
Mg#	36,5	33,3	36,7	43,3	39,2	0,5	0,4	0,4	0,6	0,5	0,5	58,1	52,5
X Wollastonite	36,77	34,96	37,25	39,13	37,77	39,85	37,58	37,01	44,40	43,40	43,11	40,93	42,90
X Enstatite	31,99	30,59	31,87	35,00	33,14	35,94	33,55	32,37	39,73	37,98	38,24	41,97	37,69
X ferrosilite	31,24	34,46	30,88	25,87	29,09	24,21	28,87	30,62	15,86	18,62	18,65	17,10	19,41
Total	100,0	100,0	100,0	100,0	100,0	100,0	100,0	100,0	100,0	100,0	100,0	100,0	100,0
X Aegirina	24,81	25,88	28,11	23,54	21,11	23,37	24,86	24,09	16,35	18,42	17,27	8,02	9,18
X jadeite	33,00	37,10	37,69	29,19	38,10	23,69	29,13	27,59	22,01	20,37	28,48	41,54	37,22
Wo + En + Fs	42,19	37,02	34,20	47,27	40,79	52,94	46,01	48,31	61,21	54,25	50,79	50,44	53,60
Total	100,0	100,0	100,0	100,0	100,0	100,0	100,0	100,0	100,0	100,0	100,0	100,0	100,0

*Omphacite crystalizing in the fracture planes resulting in micrometric garnet off-set (Fig. 7d, e)

	Microbreccia domains				Matrix M1			Matrix M2			Matrix M3		
Sample	L14-53	L14-53	L14-53	L14-53	L20-15	L20-15	L20-15	L63-15	L63-15	L63-15	L14-11	L14-11	L14-11
Generation	Omp2b	Omp2a	Omp 1a	Omp 1b	Omp2a	Omp2b	Omp2a	Omp2b	Omp2b	Omp2b	Omp3	Omp3	Omp3
SiO_2	55,57	58,52	55,73	55,92	56,31	56,86	56,65	55,49	55,72	56,33	54,72	55,44	55,77
TiO_2	0,05	0,04	0,00	0,00	0,06	0,03	0,05	0,01	0,04	0,01	0,01	0,05	0,01
Al_2O_3	7,64	9,32	10,44	11,03	9,46	7,49	8,63	7,71	7,58	8,65	2,89	5,87	2,96
Cr_2O_3	0,00	0,02	0,00	0,01	0,07	0,11	0,06	0,20	0,44	0,04	0,05	0,14	0,02
FeO	6,79	7,04	9,38	10,42	6,68	7,08	6,33	6,23	6,23	6,28	6,54	6,63	6,73
MnO	0,10	0,07	0,02	0,00	0,12	0,08	0,07	0,05	0,05	0,04	0,00	0,07	0,05
MgO	8,91	7,98	5,25	4,58	7,66	9,14	7,89	7,63	7,71	7,07	12,36	10,18	12,39
CaO	13,36	12,10	8,87	7,47	11,47	13,67	11,76	13,57	13,82	12,75	19,28	15,50	19,36
Na_2O	6,52	7,80	9,34	9,88	7,67	6,76	7,60	7,04	6,98	7,56	3,33	5,52	3,49
Total	98,9	102,9	99,0	99,3	99,5	101,2	99,0	97,9	98,6	98,7	99,2	99,4	100,8
Mg#	56,7	53,1	35,9	30,5	53,4	56,4	55,5	55,1	55,3	53,0	0,65	0,61	0,65
X Wollastonite	42,91	42,09	37,72	33,99	41,80	42,75	42,39	46,65	46,92	46,32	46,36	44,42	46,20
X Enstatite	39,81	38,60	31,09	28,98	38,85	39,79	39,61	36,50	36,44	35,75	41,35	40,58	41,15
X ferrosilite	17,28	19,31	31,18	37,03	19,35	17,46	18,00	16,85	16,64	17,92	12,28	14,99	12,64
Total	100,0	100,0	100,0	100,0	100,0	100,0	100,0	100,0	100,0	100,0	100,0	100,0	100,0
X Aegirina	10,88	8,67	20,31	20,81	9,88	12,61	9,14	11,49	11,16	9,47	9,97	11,99	9,60
X jadeite	32,22	38,18	43,99	45,54	39,60	31,11	37,35	35,40	34,85	39,24	12,46	25,04	12,62
Wo + En + Fs	56,90	53,14	35,71	33,65	50,52	56,28	53,51	53,11	53,98	51,29	77,57	62,96	77,77
Total	100,0	100,0	100,0	100,0	100,0	100,0	100,0	100,0	100,0	100,0	100,0	100,0	100,0

a later generation of omphacite (Omp2b $Di_{60}Jd_{30}Ae_8$; Fig. 10a, b), locally replacing all previous omphacite generations, is restricted to <1 mm at the clast-matrix contact; Omp2b crystals seem to follow radial infiltration patterns from the surrounding matrix into the clasts (Fig. 9d, SM8d). At the clast borders, garnet (Grt1a-b) is also overgrown, on the matrix side, by a later garnet generation (up-to 60 μm-thick mantles, Fig. 9d, SM8e), richer in FeO and MnO (Grt2a: $Grs_{18}Prp_{28}Alm_{54}$, Fig. 10a).

Veins I (i.e., crosscutting clasts but predating brecciation; Fig. 7a) are filled with Omp1b omphacite, whereas omphacite in Veins II presents an Omp2b composition.

7.2. Matrix mineral chemistry

In the microbreccia domains, fragmented omphacite and garnet crystals show compositions similar to clast minerals (i.e., Omp1a cores rimmed by Omp1b compositions and Grt1a rimmed by Grt1b). These minerals are locally sealed by interstitial Omp2a omphacite (Fig. 9c). Here, fragmented Grt1 garnet in contact with Omp2a layers are rimmed by thin (<20 μm) Mn-rich mantles with Grt2a compositions (Fig. 9d). Locally, anastomosed layers (< 70 μm thick) of Omp2b seal these microbreccia domains (Fig. SM8a).

The M1 matrix (omphacite only) is composed by about 60 vol% of Omp2b (Figs. 9d and 10a, b) crystals surrounding flake-shaped remnants of corroded, Al-richer Omp2a crystals (35 vol%), resulting in an extremely intricate mesh of both generations. The remaining 5 vol% is composed by crystals of rutiles and rare flakes of Omp1 omphacites close to the clast borders.

M2 matrix is largely made of tabular omphacite crystals of Omp2b composition, with subordinate Omp2a (mainly as crystal cores) and subordinate relics of Omp1a-b (Fig. 10a, b); composition of Omp2b is similar to the one analyzed in clasts and M1 matrix but locally noticeably enriched in Cr_2O_3 (up to 0.44 wt% vs < 0.1 wt% in the mylonitic clasts; Table 2). Garnet cores (Grt2a composition, Fig. 10c) are rimmed by almandine-poorer garnet (Grt2b; $Grs_{20}Prp_{25}Alm_{45}$). Locally, the latter, are strongly enriched in Cr_2O_3 (up to ~1 wt%), with cores showing peculiar sectorial enrichment pattern (concentrations up to 0.3 wt%; SM7e). In Grt2a, the included omphacite have Omp2a compositions, while Grt2b appear to be equilibrated with inclusions of Omp2b (Fig. 10b).

Table 3
representative major elements analysis (wt%) of garnet subdivided by microstructural domains.

	Mylonitic Fe-Ti clasts				Matrix M1				Matrix M2			
Sample Generation	L14-50 Grt1a	L14-50 Grt1a	L14-50 Grt1b	L14-50 Grt1b	L14-53 Grt2a	L14-53 Grt2a	L20-15a Grt2a	L20-15a Grt2a	L6315d Grt2b	L6315d Grt2b	L6315d Grt2b	L6315d Grt2b
SiO2	37,99	38,28	37,59	37,49	39,03	38,72	38,14	37,96	38,80	38,36	38,10	37,50
TiO2	0,03	0,06	0,19	0,09	0,09	0,09	0,06	0,07	0,06	0,09	0,05	0,06
Al2O3	21,30	20,87	20,50	20,44	21,52	21,22	21,37	21,53	21,74	19,80	20,13	19,67
Cr2O3	BDL	BDL	BDL	BDL	0,41	0,57	0,00	0,04	0,16	0,91	0,98	1,05
Fe2O3												
FeO	31,78	30,20	30,92	32,51	25,12	24,98	25,12	27,06	26,04	28,60	27,47	27,05
MnO	0,98	1,43	1,17	0,90	0,33	0,29	0,74	0,75	1,08	0,16	0,49	0,43
MgO	3,51	4,06	2,95	2,42	5,99	5,51	5,02	4,85	6,95	4,92	6,19	5,26
CaO	5,59	6,75	6,88	7,49	7,83	7,92	8,51	8,30	6,89	7,71	6,89	7,72
NiO	BDL	BDL	BDL	BDL	BDL	BDL	BDL	0,04	BDL	0,08	BDL	BDL
Total	101,2	101,7	100,2	101,4	100,3	99,3	99,0	100,6	101,77	100,63	100,20	98,70
Mg numb	9,94	11,84	8,70	6,93	0,19	0,18	0,17	0,15	21,07	0,15	0,18	0,16
Norm Grs	15,36	17,82	18,74	19,66	21,63	22,23	24,22	22,79	18,44	20,20	17,94	20,56
Norm Alm	68,32	62,20	66,18	66,97	54,99	55,84	55,85	57,61	53,88	60,32	57,13	57,88
Norm Prp	13,76	15,77	11,64	9,61	23,38	21,94	19,93	19,60	27,68	19,49	24,93	21,56
X Ca	0,15	0,18	0,19	0,20	0,21	0,22	0,24	0,22	0,18	0,20	0,18	0,21
X Mg	0,14	0,16	0,12	0,10	0,23	0,22	0,20	0,19	0,27	0,19	0,25	0,22
X Fe	0,68	0,62	0,66	0,67	0,54	0,55	0,55	0,56	0,52	0,60	0,57	0,58
X Mn	0,02	0,03	0,03	0,02	0,01	0,01	0,02	0,02	0,02	0,00	0,00	0,00

	Mylonitic Fe-Ti clasts				Veins II		Matrix M2				Metasomatic rind	
Sample Generation	I31-15 Grt1a	I31-15 Grt1a	I31-15 Grt1b	I31-15 Grt1b	I35-15 Grt1b	I35-15 Grt1b	I35-15 Grt2a	I35-15 Grt2a	I35-15 Grt2b	I35-15 Grt2b	L63-15 Grt3	L63-15 Grt3
SiO2	37,93	38,66	37,32	37,75	38,19	38,55	38,38	38,05	38,36	38,28	38,54	38,13
TiO2	0,11	0,01	0,07	0,07	0,06	0,21	0,10	0,12	0,05	0,05	0,10	0,13
Al2O3	21,32	21,47	20,95	20,71	22,15	21,20	20,91	21,14	21,40	21,41	21,30	21,02
Cr2O3	BDL	BDL	BDL	BDL	0,00	0,04	0,36	0,44	0,78	0,58	0,67	0,68
Fe2O3												
FeO	29,64	30,93	32,04	31,89	31,47	30,82	28,96	28,05	28,23	25,47	27,71	26,95
MnO	1,49	1,25	0,99	1,01	0,62	0,76	0,04	0,33	0,14	0,00	0,41	0,28
MgO	4,36	4,18	2,29	2,75	3,79	4,73	5,61	5,73	7,09	8,20	5,37	5,51
CaO	5,86	5,46	7,61	7,12	5,63	3,48	4,91	5,47	4,70	4,27	7,71	7,83
NiO	BDL	BDL	BDL	BDL	0,10	0,02	0,09	0,06	0,09	0,24	0,21	0,05
Total	100,7	102,0	101,3	101,3	102,02	99,81	99,35	99,39	100,84	98,51	102,03	100,56
Mg numb	12,82	11,91	6,67	7,93	10,76	13,30	16,22	16,97	20,08	24,36	16,23	16,98
Norm Grs	15,95	14,92	20,26	19,01	15,83	10,12	13,74	15,26	12,46	11,80	20,44	20,91
Norm Alm	63,06	66,00	66,80	66,73	69,15	70,58	64,12	62,11	59,69	56,03	58,34	57,13
Norm Prp	17,10	16,12	9,14	10,83	15,03	19,30	22,14	22,63	27,85	32,17	21,21	21,95
X Ca	0,16	0,15	0,20	0,19	0,16	0,10	0,14	0,15	0,12	0,12	0,20	0,20
X Mg	0,17	0,16	0,09	0,11	0,15	0,19	0,22	0,22	0,28	0,32	0,21	0,21
X Fe	0,63	0,66	0,67	0,67	0,68	0,69	0,64	0,61	0,59	0,56	0,57	0,56
X Mn	0,03	0,03	0,02	0,02	0,01	0,02	0,00	0,01	0,00	0,00	0,01	0,01

L: samples from Lower Shear Zone Blocks (LSZ); I: samples from Intermediate Shear Zone Blocks (ISZ); BDL: Below detection limit.

Analysis of M3 matrix eclogite-facies assemblage is difficult due to the strong greenschist retrogression (Fig. 9g). The rare omphacite relicts dispersed in the tremolite-actinolite mesh have an Omp3 composition ($Di_{70}Jd_{15}Ae_{15}$, Fig. 10a, b). No analysis could be made on lawsonite and garnet which are now completely pseudomorphosed by clinozoisite and chlorite, respectively.

In the metasomatic rinds, the newly-formed garnet is almandine-rich (Grt3: $Grs_{17}Prp_{21}Alm_{61}$, Fig. 10c).

For comparison, in the brecciated Fe-Ti metagabbros of ISZ, mylonitic clasts display the same Omp1a-Omp1b zonation found in the LSZ, with veins crystallizing Omp1b. In contrast to the LSZ, M2 matrix is composed by Omp2b in equilibrium with garnet, whose composition is comparable to Grt2a (cores) and Grt2b (rims) but slightly depleted in grossular and almandine (Fig. 10d). Locally, Cr_2O_3 content of M2 omphacite and garnets is enriched respect to those in M1, clasts and veins (1.02 wt% vs 0.35 wt% respectively).

7.3. Phase equilibrium modelling

To constrain more precisely the P-T conditions of crystallization of the Fe-Ti metagabbro mylonite and the eclogite-facies matrices, four pseudosections were modelled for samples I31–15 (mylonitic clast), L20–15A (matrix M1) and L63–15D (matrix M2) in the system NCKFMASHTO (Table 4). TiO_2 was considered due to the abundant presence of rutile in the clast of the mylonite (e.g., Fig. 8a, b, c and d). The fluid phase was assumed to be pure H_2O and was set in excess as suggested by (i) the occurrence of pseudomorphs after lawsonite (up-to 11.5 wt% H_2O; e.g., Pawley, 1994) both in clasts and (subordinate) in matrices (ii) the presence of atoll-shaped garnet (especially in the ISZ) whose crystallization may be facilitated by the presence of aqueous phases (e.g., Cheng et al., 2007) and (iii) the occurrence in metagabbro clasts of healed garnet fractures (e.g., SM9a-b), which at HP-LT is suggested to be promoted by fluid phase (Angiboust et al., 2012a; Spandler et al., 2011). CO_2 was neglected, as only small amounts of calcite occur as secondary phase in the late-stage, greenschist-facies cracks and surrounding selvages. From ICP-OS data (Table 4) molar XFe_2O_3 ratio was set to 0.20 for samples I31–15 (mylonitic clast) and L63–15D (matrix M2). Differently, ICP-OS data for sample L20–15a gave a higher molar XFe_2O_3 ratio (up-to 0.40, Table 4). Nevertheless, combining mineral modes, microprobe data and phase-equilibria modelling (SM9) the XFe_2O_3 value adopted for the P-T pseudosection of matrix M1 modelling was set again to 0.20.

For the modelling of peak mylonitic conditions (Step B in Fig. 11, sample I31–15), it was necessary to consider the sequestration of

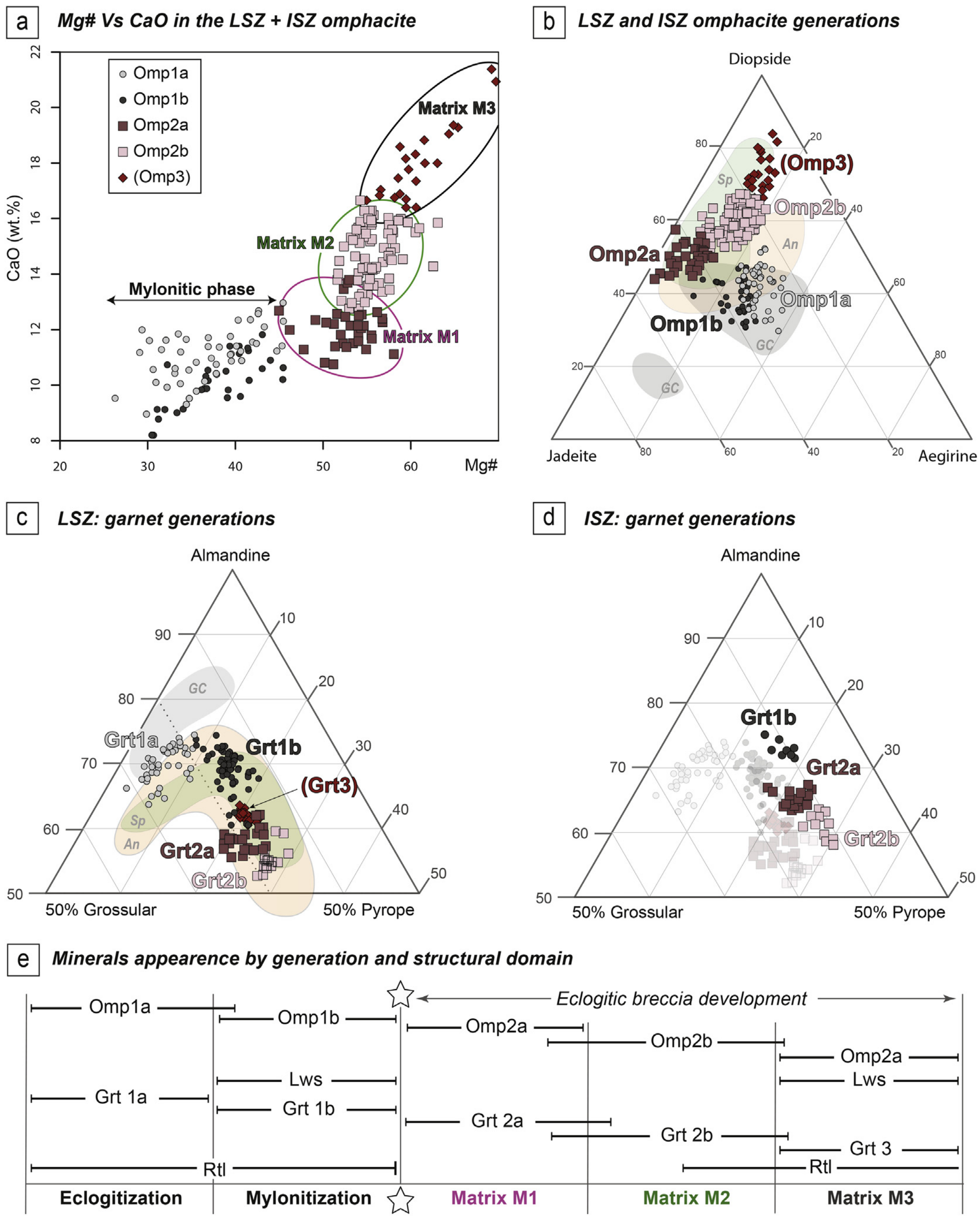

Fig. 10. EPMA composition of selected minerals: a) Mg# [MgO/(MgO + FeO)*100] vs. CaO (wt%) in LSZ + ISZ omphacites; b) Ternary-plot (Jad-Diop-Aeg) for selected omphacite from the LSZ and ISZ; c) Ternary-plot (Grs-Alm-Prp) for selected garnets from the LSZ; d) Ternary-plot (Grs-Alm-Prp) for selected garnets from the LSZ (shaded) vs selected garnets from the ISZ. Comparison with previous data from Groppo and Castelli (2010); Spandler et al. (2011); Angiboust et al. (2012a, 2014) is shown in Fig. 10 b and c; e) Evolution of the observed paragenesis with respect to microstructural domains observed in the studied samples from both LSZ and ISZ. The stars define the onset of the first brecciation event.

elements induced by the growth zonations of garnet porphyroblasts during the prograde path (Step A; e.g., Carson et al., 1999). At Step B (composition: I31–15-Gt; Table 4), the effective bulk composition was adjusted from XRF composition by removing 25% of the garnet modal abundance, following the methods of Evans (2004). This choice was supported by the small size of garnet in the sample (maximum diameter: 200 μm) and by the cross-relation existing between the observed garnet cores modal amount (~30 vol%) and the modelled amount of

Table 4
Effective bulk compositions (Mol. %) adopted for pseudosections modelling.

Sample	Stage	SiO_2	TiO_2	Al_2O_3	Fe_2O_3	FeO	MgO	CaO	Na_2O	Total
I31-15	*Mylonite-A*	52,11	3,79	7,92	2,6	10,42	9,19	10,19	3,78	100
I31-15-Grt	*Mylonite-B*	52,22	3,81	7,91	2,57	10,27	9,21	10,21	3,8	100
L20-15A	*Matrix M1*	55,59	1,18	4,39	1,5	2,28	15,74	14,72	4,6	100
L63-15D	*Matrix M2*	50,33	1,8	7,78	2,36	9,44	12,94	11,07	4,28	100

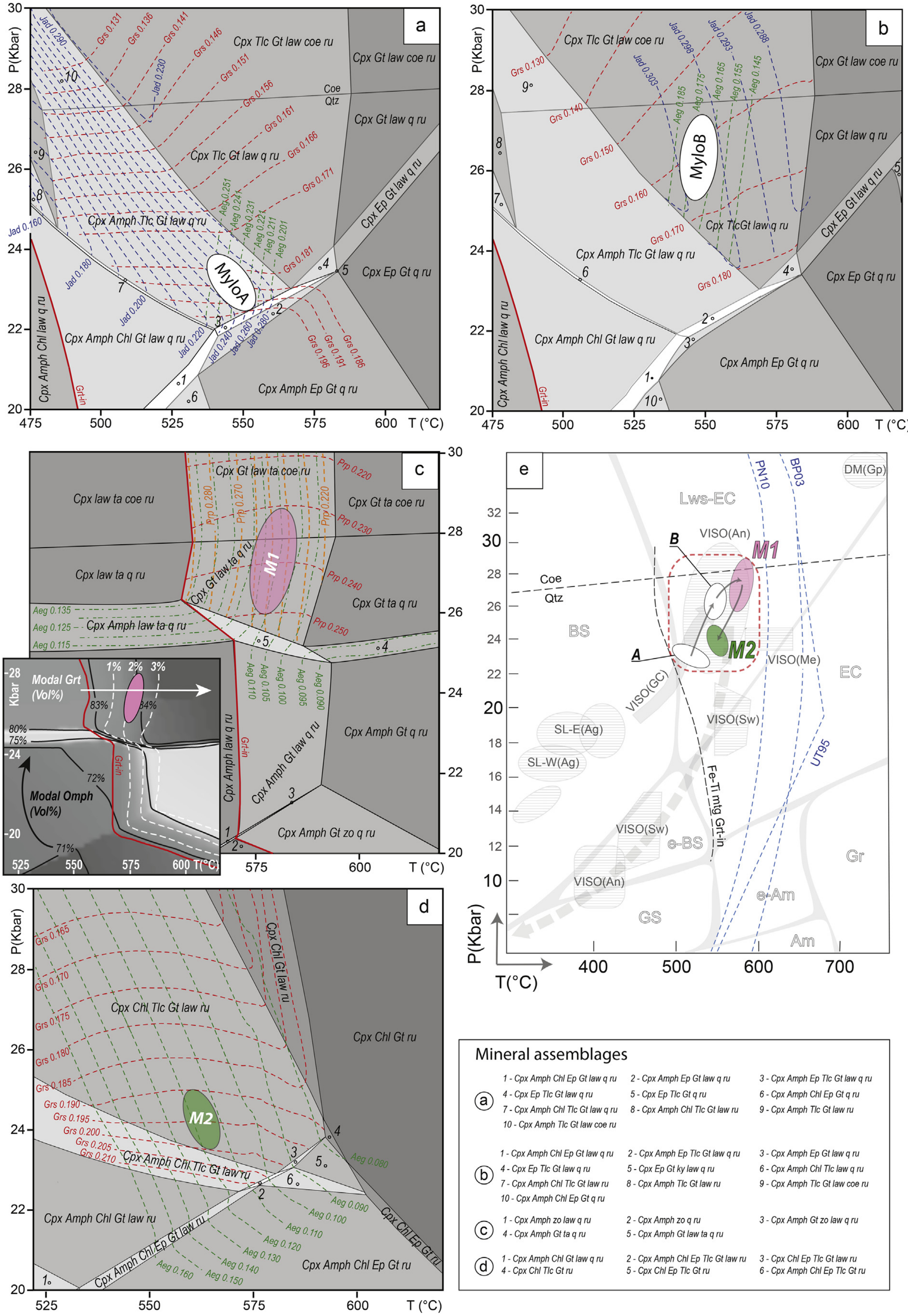
a
b
c
d
e
P(Kbar)
T (°C)
Cpx Tlc Gt law coe ru
Cpx Gt law coe ru
Cpx Gt law q ru
Cpx Tlc Gt law q ru
Cpx Amph Tlc Gt law q ru
Cpx Ep Gt law q ru
Cpx Ep Gt q ru
Cpx Amph Chl Gt law q ru
Cpx Amph Chl law q ru
Cpx Amph Ep Gt q ru
Coe
Qtz
Grt-in
MyloA
MyloB
M1
M2
Cpx law ta coe ru
Cpx Gt law ta coe ru
Cpx Gt ta coe ru
Cpx law ta q ru
Cpx Gt law ta q ru
Cpx Gt ta q ru
Cpx Amph law ta q ru
Cpx Amph law ru
Cpx Amph Gt law q ru
Cpx Amph Gt q ru
Cpx Amph Gt zo q ru
Modal Grt (Vol%)
Modal Omph (Vol%)
Kbar
Cpx Chl Tlc Gt law ru
Cpx Chl Gt law ru
Cpx Chl Gt ru
Cpx Amph Chl Tlc Gt law ru
Cpx Amph Chl Ep Gt law ru
Cpx Chl Ep Gt ru
Cpx Amph Chl Ep Gt ru
Lws-EC
VISO(An)
VISO(Me)
VISO(GC)
VISO(Sw)
BS
EC
SL-E(Ag)
SL-W(Ag)
e-BS
e-Am
GS
Am
Gr
DM(Gp)
PN10
BP03
UT95
Fe-Ti mtg Grt-in
A
B
Mineral assemblages
(a)
1 - Cpx Amph Chl Ep Gt law q ru
2 - Cpx Amph Ep Gt law q ru
3 - Cpx Amph Ep Tlc Gt law q ru
4 - Cpx Ep Tlc Gt law q ru
5 - Cpx Ep Tlc Gt q ru
6 - Cpx Amph Chl Ep Gt q ru
7 - Cpx Amph Chl Tlc Gt law q ru
8 - Cpx Amph Chl Tlc Gt law ru
9 - Cpx Amph Tlc Gt law ru
10 - Cpx Amph Tlc Gt law coe ru
(b)
1 - Cpx Amph Chl Ep Gt law q ru
2 - Cpx Amph Ep Tlc Gt law q ru
3 - Cpx Amph Ep Gt law q ru
4 - Cpx Ep Tlc Gt law q ru
5 - Cpx Ep Gt ky law q ru
6 - Cpx Amph Chl Tlc law q ru
7 - Cpx Amph Chl Tlc Gt law ru
8 - Cpx Amph Tlc Gt law ru
9 - Cpx Amph Tlc Gt law coe ru
10 - Cpx Amph Chl Ep Gt q ru
(c)
1 - Cpx Amph zo law q ru
2 - Cpx Amph zo q ru
3 - Cpx Amph Gt zo law q ru
4 - Cpx Amph Gt ta q ru
5 - Cpx Amph Gt law ta q ru
(d)
1 - Cpx Amph Chl Gt law q ru
2 - Cpx Amph Chl Ep Tlc Gt law ru
3 - Cpx Chl Ep Tlc Gt law ru
4 - Cpx Chl Tlc Gt ru
5 - Cpx Chl Ep Tlc Gt ru
6 - Cpx Amph Chl Ep Tlc Gt ru

garnet crystallized at StepA (~24 vol%). Such subtraction was not performed for matrices M1 (L20–15A) and M2 (L63–15D), as the absence of any remnants of prograde mylonitic garnet Grt1a and Grt1b from the matrices suggests a complete dissolution/reaction of the pre-existing minerals, thus excluding element sequestration and/or local bulk-effects.

The P-T pseudosections were calculated with Perple_X (software version 7.7.5; Connolly, 2005, Connolly, 1990) with the internally consistent thermodynamic dataset hp04ver.dat (Holland and Powell, 1998; Holland and Powell, 2003). Mineral solid-solution models were Omph(GHP) for omphacite (Green et al., 2007), Ep(HP) for epidote/clinozoisite (Holland and Powell, 1998), Gt(HP) for garnet (Holland and Powell, 1998), cAmph (DP) for amphibole (Diener et al., 2007), Chl(HP) for chlorite (Holland and Powell, 1998), feldspar for ternary feldspar (Fuhram and Linsley, 1988) and the ideal solutions T for talc. H_2O-CO_2 fluid solution model was from Holland and Powell (1991, 1998).

The pseudosections for sample I31–15 (step A) and recalculated bulk I31–15-Grt (Step B) are dominated by tri- and quadrivariant fields, with a few di- and quini-variant fields, and are shown in Figs. 11a-b. The P-T conditions were constrained by comparing predicted garnet and omphacite isopleths with selected mineral compositions (Tables 2 and 3). All the boxes on Figs. 11a-d incorporate typical uncertainties on EMPA analyses, ~3% to ~5% (Lifishin and Gauvin, 2001). StepA, as defined by mylonitic garnet core composition Grt1a and included omphacite Omp1a (Tables 2 and 3), is marked by thermodynamic equilibrium at ~2.3Gpa and ~530 °C (Figs.11a and 11e). The mylonitic peak conditions (StepB: ~2.6 Gpa, ~550 °C; Figs. 11b, e) is constrained by using the mylonitic garnet rim compositions (corresponding to Grt1b; Table 3) which have the lowest XGrs content and coincide with the highest XJad content observed for omphacite Omp1b (Table 2). The PT conditions for M1 matrix (~2.7 GPa, ~580 °C; Figs. 11c, e) were constrained by the compositions of the Mn-rich garnet rims (Grt2a; Fig. 9d) crystalizing at equilibrium with the omphacite Omp2a at the sharp transition clast-M1 matrix (e.g., Fig. 9d; compositions in Tables 2 and3). Remarkable agreement exists between the modelled modal volume of garnet (~1–2%vol) and the one observed in the rocks (~1%vol, Fig. 9d), supporting the accuracy of the pseudosection modelling.The later-stage M2 matrix (Figs. 11d, e) is marked by pressure of ~2.4 GPa and temperature of ~560 °C (Fig. 11d); considering the analytical errors and the modelling incertitude, such metamorphic conditions are totally comparable to those of the mylonitic steps A-B and M1 matrix (Fig. 11e). Mineral compositions used to constrain M2 matrix were garnet Grt2b and included omphacite Omp2b, the latter marked by a decrease in XJad and the relative enrichment in XDiop (Fig. 10b).

8. Discussion

8.1. Evidence for brecciation at eclogite-facies conditions

Based on (i) petrographic observations on Monviso Fe-Ti metagabbros, (ii) P-T estimates for the Lago Superiore Unit (~550 °C, 2.6–2.7 GPa) and (iii) macrotextural relationships at the block scale, Angiboust et al. (2012a) interpreted the Monviso breccias as marking eclogitic brittle rupture, thereby potentially reflecting intermediate-depth seismicity. Nevertheless, from structural and stratigraphic observations, (Balestro et al., 2014; Balestro et al., 2015a) and (Festa et al., 2015) interpreted some breccia blocks dispersed in the LSZ as relict sedimentary and tectonic breccias inherited from a Tethyan Oceanic Core Complex, as for several Alpine ophiolites (e.g., Central Alps: Desmurs et al., 2001; Western Alps: Manatschal and Müntener, 2009; Corsica: Marroni and Pandolfi, 2007). Polymictic breccia can indeed be observed as conglomeratic horizons containing well-rounded fragments and boulders of metagabbro, metabasalt and serpentinite (Fig. SM2) embedded in a strongly deformed, sedimentary-derived mylonitic matrix (SM2b). However, they are always intercalated with the metasedimentary lenses scattered in both the ISZ and LSZ (Figs. 3a, b) and their mafic fragments are never brecciated.

The following observations confirm that the ('eclogitic') breccia dispersed in the LSZ are of a different sort and were formed during eclogite facies conditions:

(1) Mylonitization of the Fe-Ti gabbros predating brecciation takes place under eclogite facies. Evidence that foliation of the clasts forms at eclogite facies conditions is shown by i) the growth of *syn*-kinematic garnet (Fig. 8a, b) marked by ubiquitous pressure shadows (Fig. 8a), ii) the folding of rutile crystals, iii) the irregular boundaries of omphacite crystals indicating grain-boundary migration processes, iv) their large aspect ratio (up to 1:15) and v)the occurrence of CPO for omphacite grains (Figs. 8a, b).. All these observations testify to processes of dynamic, ductile deformation accompanying eclogite-facies mylonitization (steps A and B in Fig. 11) and rule out topotactic, strain-free recrystallization of a foliation inherited from oceanic stages (except in rare un-brecciated Fe-Ti blocks; e.g., LSZ 28–15; Fig. 8d). This is in agreement with earlier conclusions by (Philippot and Kienast, 1989; Philippot and van Roermund, 1992).

(2) All eclogitic breccia planes preserved in the metagabbro blocks for ~15 km along strike of the LSZ cut across mylonitic eclogite facies foliation. At the outcrop scale, breccia intersects abruptly, at various angles, the eclogitic foliation made of intact Mg-Al metagabbros and Fe-Ti metagabbro boudins (e.g., Type 2 blocks; Figs. 4e, f, g, h and 6a, b). At the thin-section scale, brecciation cuts across syn-kinematic garnet (Grt1a-1b; Figs. 8g and 9a, b) and rutile trails aligned along the mylonitic foliation (Figs. 8f, 9a-b).

(3) Within breccia planes, the matrices of the un-foliated clast-in-matrix structure (with straight grain boundaries, common triple-point junctions and only minor evidence for undulose extinction in omphacite grains), contain typical eclogite facies paragenesis (e.g., Figs. 8f and 9). Their P-T estimates (Fig. 11) testifies to brecciation at eclogite facies conditions (M1: ~2.7 GPa, ~580 °C; M2: ~2.4 GPa, ~560 °C). The existence of successive, discrete brittle events at eclogite-facies conditions is demonstrated by (i) the clear crosscutting relationships between the mylonitic metagabbros and the matrices (e.g., Figs. 4c, d and 7a, b, c, d) as well as (ii) the many tension gashes and dilatant veins filled with omphacite (Omp1b) ± apatite found in clasts and metagabbro wall rocks (Figs.4g and 7a). These latter cut across the pre-existing mylonitic foliation and are post-dated by eclogite-facies matrices crystallization (Fig. 7a).

Fig. 11. P-T estimates for the studied eclogites, inferred from PerpleX pseudosection modelling in the system NCKFMASHTO; StepA-B, M1 and M2 boxes consider ca. 5% calculated uncertainties. Effective bulk composition in Table 4. Abbreviations: Omph, omphacite; Grt, garnet; Jad, jadeite; Aeg, aegirine; Grs, grossular; M1, matrix M1; M2, matrix M2; A and B, mylonitic steps. (a-b) P-T estimates for the prograde mylonitization of Fe-Ti metagabbro. Step A: crystallization of Grt1a and Omp1a; Step B: crystallization of Grt1b and Omp1b. Bulk and mineral compositions obtained from sample ISZ 31–15 (Tables 2, 3 and 4). (c) P-T estimates for the crystallization of M1 matrix. Bulk and mineral compositions obtained from sample LSZ 20–15a (Tables 2, 3 and 4). In the box: modelled modal volumes of omphacite (black lines) and garnet (white, dotted lines). (d) P-T estimates for the crystallization of M2 matrix. Bulk and mineral compositions obtained from sample LSZ 63–15D (Tables 2, 3 and 4). (e) Estimated P-T trajectory from pseudosection modelling, integrated with the estimations from previous works on the Monviso, Schistes Lustrés and Dora Maira areas. The red, dotted-line box represents the PT estimates considering uncertainties on bulk composition; the thin, gray arrows suggest the relative chronology of crystallization obtained by structural evidences. SL-W(Ag), SL-E(Ag): West and East Schistes lustrés: Agard et al. (2009). VISO(GC): prograde eclogitization P-T path of Monviso metagabbros: Groppo and Castelli (2010). VISO(An): Lago Superiore Unit, Monviso: Angiboust et al. (2012a) for peak and retrograde conditions; VISO(Me); Monviso metagabbros: Messiga et al. (1999). VISO(Sw): Monviso metagabbros and metabasites: Schwartz et al. (2000) for peak and retrograde conditions. Dotted line: inferred retrograde P-T path for the Lago Superiore Unit (Angiboust et al., 2012a). Blue, dotted lines represent the experimental dehydration curves for antigorite; BP03, Bromiley & Pawley (2003); UT95, Ulmer & Trommsdorff (1995) UT95); PN10, Padrón-Navarta et al. (2010).

The sedimentary origin of these eclogitic breccias can be refuted for the following reasons:

(1) eclogite breccias lack clastic material (e.g., quartz, phengite, serpentinite or talc grains; Figs. 4, 7a, b, c, d, 8c and 9b, c, d) and are essentially monomictic (omphacite ± garnet ± lawsonite), by contrast to what is observed in the polymictic Monviso metasedimentary conglomerates (e.g., SM2a-b; see also Balestro et al., 2015a, 2015b);

(2) clast analysis (Fig. 6c, d) and the progressive dismantlement from the fresh rock to the breccia cores (Fig. 6a, b) indicate that part of eclogitic breccias are tectonic. Preserved breccia planes indeed advocate for dynamic fracturing, as they record the full classical rim-to-core sequence (Jébrak, 1997; Mort and Woodcock, 2008) from intact metagabbro to fractured rock, crackle breccia, mosaic breccia and chaotic breccia (i.e., blocks B154, B1 and B77; Figs. 6a, b, c);

(3) eclogite breccias are essentially monogenic (see above; e.g., Figs. 4c, 6a, b and 7a, b, c, d). Clasts of Mg-Al metagabbros are indeed restricted to the rims (20–50 cm zones) of breccia planes cutting across the contact between Fe-Ti-gabbro and Mg-Al-gabbro (which is observed in <10% of the blocks) and rapidly disappear towards the core of breccia planes. By contrast, breccias formed by oceanic detachment faults exhuming oceanic core complexes may exhibit a larger compositional variety in the fragments (metabasalts, metagabbros, metaperidotites, sometimes embedded in metasediments; e.g. Escartín et al., 2003, 2001). Whenever monogenic breccias are observed, as in hyperextended margins (e.g., Desmurs et al., 2001), their clasts preserve magmatic fabrics and/or foliation develops in the surrounding matrix, which is never observed in Monviso eclogitic breccias (e.g. Figs. 7c, 8f, and 9d, e, f).

It is therefore possible to distinguish two types of breccias in the Lago superiore unit:

— the Fe-Ti metagabbro breccia blocks formed at eclogite-facies conditions (as first proposed by Angiboust et al., 2012b, Angiboust et al., 2011).

— the conglomeratic/breccia layers found associated to metasedimentary slivers (which can be ascribed to pre-Alpine, pre-subduction tectonic and/or sedimentary processes, as first proposed by Balestro et al., 2014).

8.2. Reconstructing the discrete steps of eclogitic brecciation

Structural/microstructural relationships, mineral chemistry data on breccia matrix and clasts and phase equilibrium modelling together with previous observations from the literature (Angiboust et al., 2012a; Philippot, 1987; Philippot and Kienast, 1989; Philippot and Selverstone, 1991; Schwartz et al., 2000; Spandler et al., 2011), allow to recognize several episodes in the brecciation process at eclogite facies conditions. Based on the P-T estimations by pseudosection modelling (Fig. 11) and the successive omphacite and garnet compositions (Fig. 10), these steps can be ascribed to prograde to peak mylonitization (Fig. 12; StepA-C) and early retrograde stage linked to exhumation (Fig. 12; steps D to E).

- *Eclogitization and mylonitization prior to brecciation* (steps A and B):

The Fe-Ti and Mg-Al gabbros (either within the crustal sequence or intruded in the peridotitic mantle) underwent prograde eclogitization (step A, ~23 kbar/~530 °C; Fig. 12), as inferred by phase equilibria on garnet and omphacite cores (respectively Grt1 and Omph1) from both mylonitic clasts (e.g. Figs. 8a-c) and low-strain, unbrecciated Fe-Ti metagabbros (type 3 blocks, Fig. 8d). In the latter, topotactic replacement of pre-existing magmatic clinopyroxene crystals by omphacite (Omp1a) associated to rutile (growing after magmatic ilmenite) and coronitic garnet Grt1a after plagioclase can be observed (Figs. 8d).

Progressive ductile deformation (step B, ~26 kbar/~550 °C; Fig. 12) is attested by the formation of a mylonitic foliation, with newly grown omphacite (Omp1b) as rims around Omp1a and coeval growth of Grt1b around Grt1a garnet cores (with Omp1b inclusions in Grt1b), grain size reduction, fracturing and dismembering of the omphacite pseudomorphs after magmatic clinopyroxene. This is accompanied by the progressive flattening of rutile ribbons in extremely elongated trails parallel to the foliation. Garnet underwent fracturing, especially where segregated into bands or lenses (Figs. 8g), possibly as a result of indentation between garnet crystal borders and/or hydrofracturing (as suggested by Spandler et al., 2011). This step was accompanied by the (probably transient) development of tension gashes and dilatant veins with Omp1b omphacite ± apatite.

- *Brecciation* (steps C to E):

The first brecciation event (step C), coincident with the relative rotation of clasts of Fe-Ti (and rare Mg-Al) metagabbros, is recorded by thin (< 200 μm-thick; Fig. 8f) inter-clast domains filled with either dismembered and re-oriented grains from clasts ("microbreccia" domains) or newly crystallized, ipidiomorphic omphacite-rich (Omp2a) M1 matrix (Fig. 9d). In both matrix types, this stage is associated to volumetrically limited Grt2a overgrowths around mylonitic garnets (Figs. 9d and 11c). In the microbreccia domains, fractured and angular omphacite and garnet exhibit strong grain size reduction, obliteration of foliation, and compositions similar to minerals in clasts: all these features show that they correspond to clast pieces brittlely-deformed during brecciation and subsequently sealed by interstitial omphacite Omp2a and associated Grt2a rims (Fig. 9c and SM8a). Pseudosection modelling suggests equilibrium of matrix M1 at ~27 kbar/~580 °C, so that the onset of brecciation took place at the peak P-T conditions reach by the LSU metagabbros (Fig. 12).

The crystallization of Omp2b in both the microbreccia and M1 matrix domains (developing complex, radial-shape infiltration patterns overgrowing the pre-existing omphacite grains; Figs. 9d and SM8b) testifies a later-stage fluid infiltration, tentatively ascribed to the crystallization of the M2 matrix. In this latter the same assemblage is recorded, with euhedral Omp2a rimmed by Omp2b (locally Cr-rich) associated to garnets showing Grt2a cores and Grt2b rims (the latter including Omp2b crystals) with sectorial Cr-enrichment patterns. From structural relationships (Figs. 7a, b) it is possible to infer that the crystallization of M2 matrix (~24 kbar/~560 °C: Step D in Fig. 12) took place after the development of both microbreccia and M1 matrix domains.

A third, volumetrically dominant (80 vol%) lawsonite-rich M3 matrix crosscuts all preexisting structures (Step E Fig. 12; Fig. 7b). The abundance of lawsonite pseudomorphs in M3 (up to ~40 vol% in places), compared to the rather dry assemblages of M1 and even M2, advocates for late-stage massive fluid infiltration, most probably externally-derived (e.g., from serpentinite and metasediment dehydration at deeper levels, in agreement to what observed on HP-veins by Spandler et al., 2011 or on blocks metasomatic rinds by Rubatto and Angiboust, 2015), since no significant dehydration is predicted for Fe-Ti eclogitic metagabbros at such PT conditions (i.e., not until lawsonite breakdown). We speculate that the infiltration of fluids may have been promoted by the first steps of brecciation (steps C and D) by mechanical weakening and porosity increase. Due to the impossibility to retrieve the original chemical composition of the M3 matrix, P-T constraints for this stage are assessed using relative chronology (e.g., M3 postdating M2; Fig. 7b) and lawsonite stability.

- *Post-brecciation evolution* (step F):

Step F corresponds to the alteration visible in the rims of brecciated blocks, i.e. subsequent rind formation (up to 0.5 m thick) at their contact with the antigorite-rich matrix embedding them in the LSZ (Figs. 4b, 7d). Rind formation affects both clasts and matrix, and thus postdates

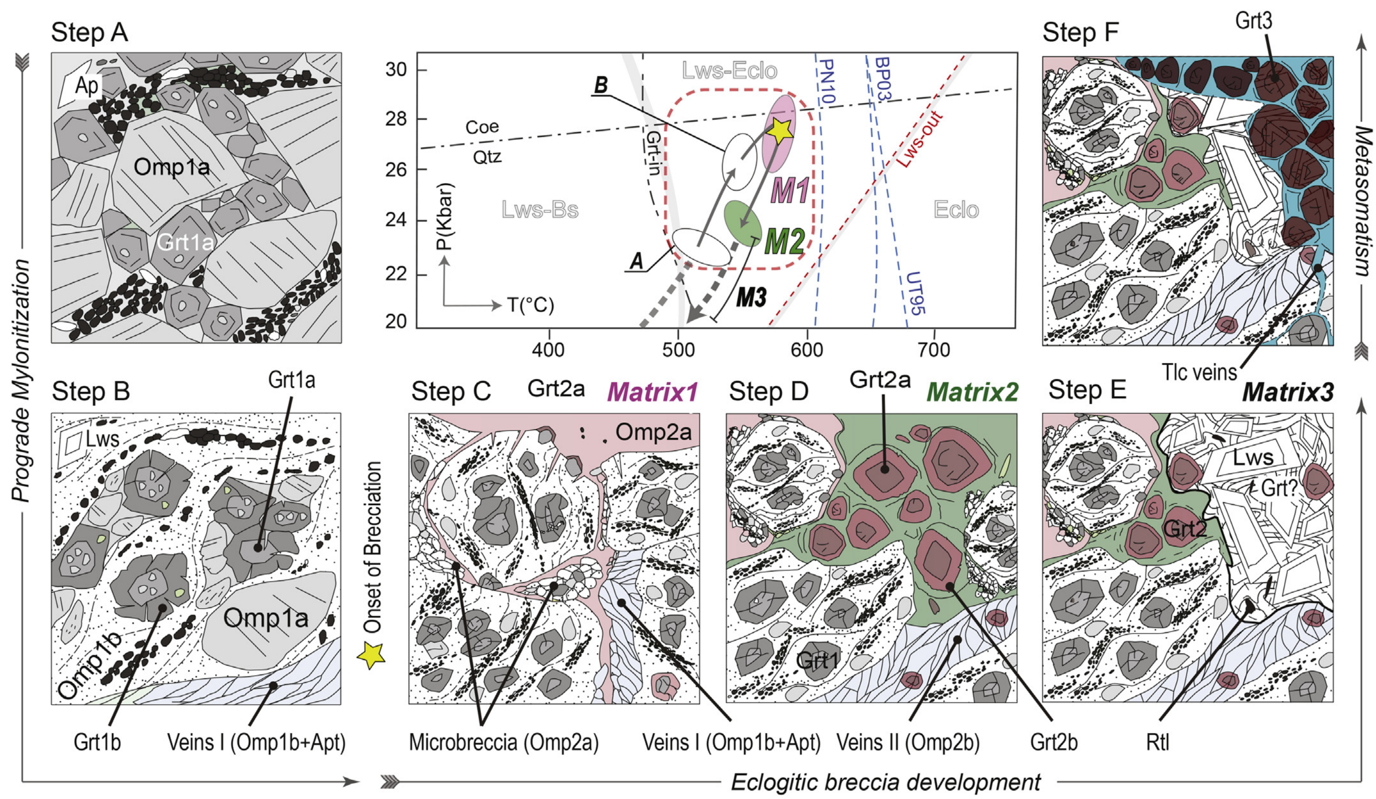

Fig. 12. Relative chronology of events (with associated P-T position) leading to the brecciation of eclogite-facies Fe-Ti metagabbros from the LSZ. Eclogitized igneous texture (step A) are progressively obliterated by mylonitization (step B), with related opening of Omp1b ± apatite veins I. Various amount of hydrous minerals grew at this stage (e.g., lawsonite). Progressive deformation culminated in the first brecciation event (Step C), with brittle disruption of metagabbros (e.g. formation of crackle breccia domains and micro-displacement of garnets), clasts rotation and crystalization of the omphacite-rich matrix M1. On-going deformation and increasing water-content of circulating fluids led to the crystallization of matrices M2 (Step D, omphacite + garnet) and M3 (Step E, lawsonite + omphacite + garnet). Localized metasomatism (with crystallization of newly-formed garnet + talc + chlorite + amphibole + Ca-rich diopside) occurs after all the previous events (Step F). The red, dotted-line box represents the PT estimates considering uncertainties on bulk composition; the thin, gray arrows suggest the relative chronology of crystallization obtained by structural evidences.

brecciation. In metagabbro block rims, the preexisting eclogitic facies assemblage is replaced by talc, chlorite, Grt3 garnet, sodic amphibole, diopside, rare phengite and lawsonite pseudomorphs indicative of (externally derived) fluids. Chemical alteration rapidly decreases from block rims to cores. These rinds form in the LSZ after peak burial and brecciation, during exhumation (Fig. 12a; see also Angiboust et al., 2014).

Late-stage retrogression of the eclogite-facies blocks into a greenschist facies assemblage (i.e., tremolite-actinolite, chlorite, epidote, and mm-thick veins of calcite + albite + quartz + epidote; Fig. 9g and SM7b, c, d) is widespread in metabreccia blocks. The dryer matrices (M1 and M2) and less permeable clasts underwent only partial retrogression at their rims and better preserved their pristine eclogite-facies assemblages.

8.3. Locus of brecciation and progressive strain localization along the slab interface

8.3.1. Strain localization along Fe-Ti gabbro horizons

In the Monviso metaophiolite brittle deformation and brecciation at eclogite-facies conditions took place preferentially along Fe-Ti metagabbro horizons and in their vicinity (as shown by the largely monogenic nature of breccia blocks), hence in the most resistant rocks, considering field observations (i.e., strain partitioned in folded Mg-Al metagabbros and serpentinites) and available flow laws. At metamorphic peak conditions reached by the Lago Superiore Unit (~27 kbar/580 °C, brecciation step C; Fig. 11e), the strength of eclogitic Fe-Ti metagabbros may indeed be up to 7 GPa (see Jin et al., 2001 for a comparable assemblage made of 50% garnet, 40% omphacite and 10% quartz) while no available data exist to describe the behaviour of Mg-Al metagabbros. Nevertheless, taking in account the strong dependency between garnet volume fraction and the strength of the rock (Jin et al., 2001), we can approximate that of the garnet-free Mg-Al metagabbros up-to one order of magnitude lower than those of Fe-Ti metagabbros.. Thus, the strength of Fe-Ti metagabbros exceeds the one of both Mg-Al metagabbros and serpentinite (whose effective viscosity is ~4 orders of magnitude lower than metagabbros; e.g., Hilairet et al., 2007).

Is a matter of fact that the Fe-Ti metagabbro boudins embedded inside the in Mg-Al gabbros represent a strong rheological contrast that may explain brittle rupture localization, as seen at the boundaries between multi-layered lithologies/media with different competency (e.g., Strömgård, 1973; Treagus, 1981). Nevertheless, the behaviour of multi-phase material is not very well-known (e.g., Schüler et al., 2013) and that of monomineralic layers may deviate from flow laws: the strength of pure omphacite is for example twice lower than that of eclogite and four-time lower than garnetite (e.g., the "omphacitite" of (Jin et al., 2001). Thus, we speculate that the almost pure Omp (+/−Ap) bearing veins developed during prograde mylonitization (Figs. 7a, 8e, f and SM8a; see also Philippot, 1987, Philippot and Kienast, 1989 and Philippot and van Roermund, 1992) may have acted as weaker layers that localized brecciation, as suggested by the preferential development of microbreccia domains at vein-clast boundaries (e.g., Fig. 8f). Moreover, "semi-brittle" modes of deformation, involving mechanical failure at the contact between monomineralic and polymineralic media, as observed in experiments on clinopyroxene and garnet (Kirby and Kronenberg, 1984; Philippot and van Roermund, 1992; Rutter, 1986), might explain the rheological processes leading to brecciation. Ongoing reactions are also likely to modify these rheologies - i.e., the growth of garnet (along with fluid release) in Mg-Al metagabbros - likely increased the strength (and brecciation potential) of this lithology.

8.3.2. Progressive strain localization within the slab

Field mapping (Figs. 3a, b, SM1) shows that most of the breccia blocks (88% of Type 2 blocks and all Type 1) are concentrated in the upper part of the LSZ, below the Mg-Al gabbro horizon but above the large slivers of Mg-Al metagabbros (Figs. 5a, b). Their structural position is the same all along strike of the LSZ, from Colle di Luca to Ghincia Pastour (~15 km; Fig. SM1). Brecciation therefore occurred predominantly (i) along dykes and sills of Fe-Ti metagabbros emplaced within and towards the base of the Mg-Al metagabbro sequence (i.e. in the future LSZ; Figs. 3b and 13a, b) and to a lesser extent (ii) within Fe-Ti metagabbros sandwiched between the Mg-Al metagabbro and metabasalts layers (i.e., along the future ISZ). This advocates for brecciation in both the LSZ and ISZ, rather than a single brittle event in the ISZ with subsequent incorporation into the LSZ (as initially envisioned by Angiboust et al., 2012b).

Progressive deformation across the LSZ and ISZ is shown in Fig. 13. Location of brecciation was controlled by the strength contrast across the lithological sequence (§ 8.3.1) and assisted by further strain localization and fluid circulation into the Fe-Ti metagabbros (Fig. 13a). The eclogitic breccias, at least during the early stages of LSZ development, thus acted as a major mechanical discontinuity. Formation of the M1 matrix (Fig. 13a) marks the onset of brecciation at peak P-T conditions (~27 kbar/580 °C) and testifies to changes in porosity/permeability, progressively enhanced in M2 and (mostly) in M3 matrices (Figs. 12 and 13a). The presence of the Lws-rich M3 matrix assemblage (Figs. 7b and 9g), which requires extensive fluid infiltration, indicates that eclogite breccias formed near the base of the Mg-Al metagabbro horizon became connected at that stage.

Strain localization in metagabbros(testified by their pervasive mylonitization and following brecciation) indicates that serpentinization of the top of the mantle section was initially insufficient to localize all ductile strain. It is likely, however, that serpentinization progressively extendedinto the peridotite sole and finally localized most of the strain in the LSZ, as suggested by.

(i) the partly rodingitized, unbrecciated Fe-Ti gabbro intrusions found in the basal peridotite (Figs. 3a-b and SM1; as in active slow-spreading oceans, e.g., the SW Indian Ocean and Mid-Atlantic ridges; Dick et al., 2008; Lagabrielle and Lemoine, 1997; Lissenberg et al., 2009; Lagabrielle and Cannat, 1990) resemble Type 3 unbrecciated Fe-Ti metagabbro blocks, which are restricted to the lower part of the LSZ (Figs. 5b and SM1) and which size increases towards the serpentinite sole; these blocks thus likely correspond to sills/dykes initially emplaced into the peridotite sole and later incorporated into the LSZ during its progressive thickening (Fig. 13a).

(ii) incorporation of unbrecciated Type 2 and Type 3 metagabbro slivers/blocks into the LSZ (and to a minor extent in the ISZ; Figs. 4a, 5 and 13a), suggestive of progressive, fluid-assisted network widening of the shear zone (e.g., Means, 1995) and local tectonic reworking of the crustal organization (Fig. 13a, b).

(iii) dissemination of eclogitic metagabbro blocks in the LSZ and ISZ occurred after the metamorphic peak (i.e., during early exhumation stages and after the eclogite-facies brecciation) likely at the eclogite to blueschist facies transition (Angiboust et al., 2014). We speculate that the source for the fluids driving the progressive serpentinization (and weakening) of peridotites derived from deserpentinization processes at deeper slab levels (as already stated by Spandler et al., 2011 or Angiboust et al., 2014). The interaction between these fluids and metagabbros led also to the post-brecciation rind formation (SM7d), with massive recrystallization of talc, chlorite, subordinate Cr-rich garnet (Gt3), serpentinite (plus sodic amphibole and accessory phengite).

Interestingly, the presence along the LSZ of isolated lenses of metasediments requires hm-km offsets along an initially discontinuous oceanic crust (Fig. 13a). We propose that such lenses may be inherited from the initial seafloor structure (with little lateral continuity compared to other shear zones interpreted as remnants of oceanic core complexes; e.g., Corsica; Lagabrielle et al., 2015) or correspond to extreme boudinage. The amplitude of the offsets is nevertheless limited by (i) the fact that eclogitic breccia planes are always found on the upper/western side of the Mg-Al metagabbro Type 2 slivers, broadly parallel to the LSZ shear zone walls (e.g., Punta Murel and Colle di Luca; Figs. 3b, 4a, 5a, SM1) and (ii) the ordered distribution of eclogitic breccia blocks in the upper part of the LSZ (Fig. 5a, b and SM1), which both advocate for only small displacements after their dissemination.

Final detachment of the Lago Superiore Unit took place in a shear zone located further below(i.e., the Basal Shear Zone; Fig. 13a, b).

8.3.3. Brecciation mechanism: triggered by earthquake or hydrofracturation?

Angiboust et al. (2012a) argued that the switch from ductile to brittle regime documented by eclogite brecciation (crosscutting the eclogitic mylonitic foliation) could result from either a change in strain rate (i.e., following an earthquake) or/and in fluid pressure (whether or not by dehydration embrittlement; Hacker et al., 2003b). The fluid ingression recorded by the M3 lawsonite-rich matrix (Lws~40 vol%) could thus be seen either as a consequence or as the trigger for strain localization.

Evidence for instantaneous deformation includes the sharp breccia planes crosscutting the eclogitic mylonitic foliation, the formation of crackle-breccia with relative displacement (and the full transition from crackle to chaotic breccia), the formation of microbreccia domains and the existence of minerals fractured and offset along omphacite-bearing planes (e.g., garnets; Fig. 8g).

It is impossible, at this stage, to assess whether eclogitic brecciation was coseismic: the lack of seismically-derived structures/microstructures (e.g., pseudotachylites), the limited extension of the breccia planes preserved in the blocks (< ~3–4 m) and the unknown duration of brecciation call for caution in relating breccias to earthquakes. It is interesting, however, to note that in Corsica, pseudotachylites are found in a similar structural position as the eclogite breccias, i.e. in metagabbros and peridotites at and above the Moho (Deseta et al., 2014; Magott et al., 2016). Elucidating the nature of infiltrating fluids and the deformation mechanism acting in the Fe-Ti metagabbros (work in progress) may provide further information and help decide which of the two processes was most effective.

9. Conclusions

This study documents progressive strain localization within the slab into the gabbroic crust during and prior to the detachment of the large Monviso slab fragment:

(1) In metagabbro blocks outcropping inside the LSZ, the majority of breccias formed by brittle rupture under eclogite-facies conditions. By the occurrence of eclogite-facies mylonitic Fe-Ti and Mg-Al metagabbro clasts we exclude their origin by sedimentary deposition in paleo-oceanic basins or high-pressure overprinting of breccia formed at shallow crustal depths. The lack of deformation in the matrix between eclogite clasts contrasts with the reworked matrix of other (pre-Alpine) metasedimentary slivers dispersed in the shear zone.

(2) Brecciation controlled the initial stages of strain localization within the LSZ. It preferentially occurred in Fe-Ti gabbros embedded in Mg-Al metagabbros, suggesting that the rheological contrast between the two metagabbros controlled the onset of brecciation.

(3) A complex succession of events accompanied brecciation. The existence of three successive types of matrix, with a sharp increase

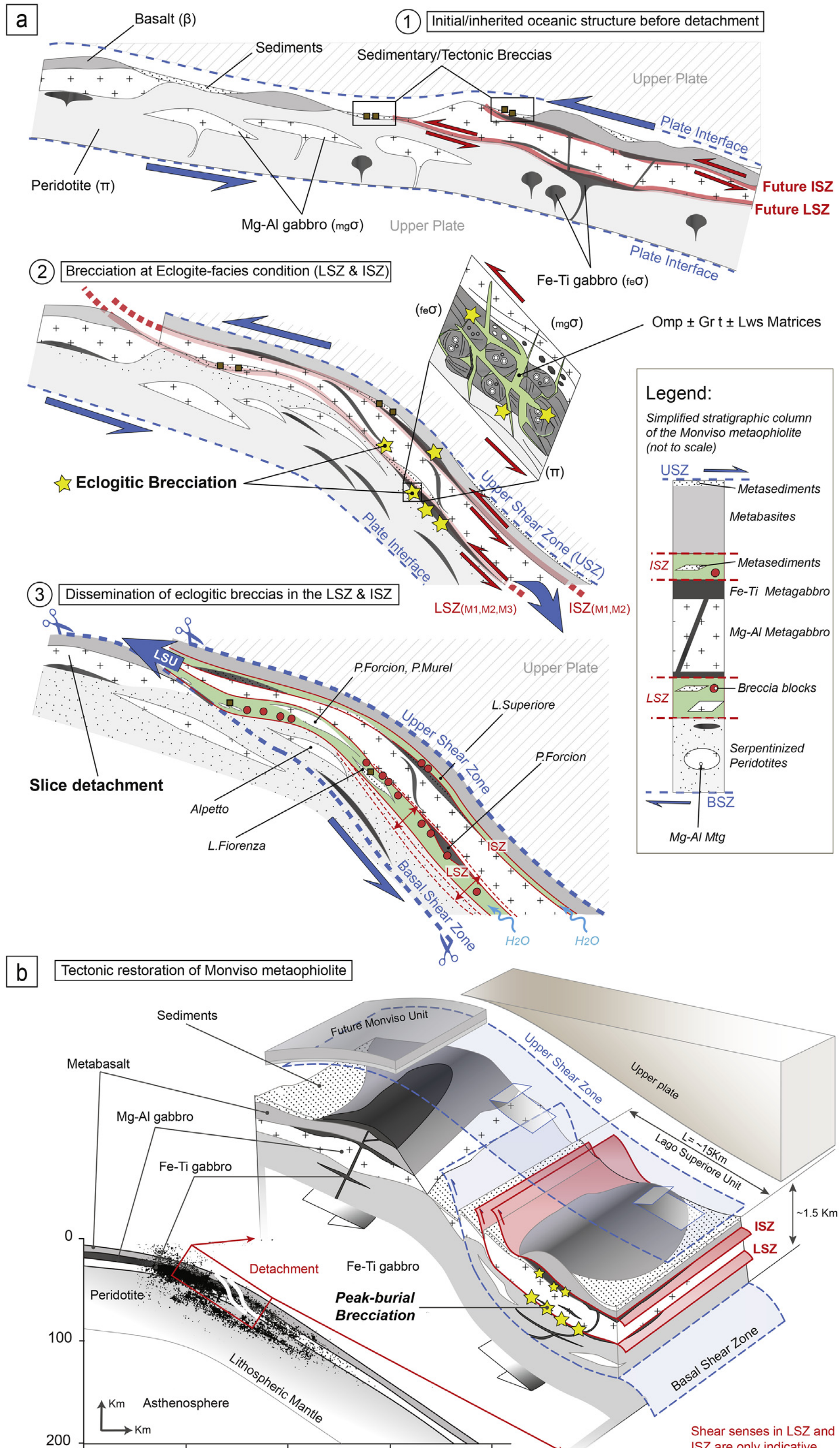

Fig. 13. (a) Localization of the brecciation events inside subducted oceanic crust (corresponding to the Monviso LSU) and its implication. At pre-subduction conditions (Stage1) the slow-spread oceanic crust is characterized by a complex intrusion pattern of Fe-Ti gabbros (e.g., as suggested by Lagabrielle, 2009). During subduction it reached eclogite-facies conditions (Stage2) and the increasing deformation coupled to the rheological contrast between Fe-Ti and Mg-Al metagabbros culminate at peak-burial conditions in the brittle failure (brecciation) mainly in the Fe-Ti metagabbros. As suggested by the crystallization of matrices progressively richer in water (M1: pure omphacite. M2: omphacite + garnet. M3, 70% of volume composed by lawsonite) and the subsequent development of metasomatic rinds and veins, brecciation likely promote the generation of porosity supporting the external fluid infiltration (Stage3). The interplay between on-going deformation and the fluid-assisted metasomatism likely decreased the strength of the rock, promoting the widening of the shear zones and the detachment/dissemination of blocks and slivers into the serpentinized LSZ and ISZ (Stage 3). (b) Schematic 3D tectonic restoration of a plate interface at intermediate depth inferred from the structures observed in the Monviso metaophiolite, with the locus of the eclogite-facies brecciation (yellow stars) and the localization of the main shear zones.

in fluid-content for the latest, lawsonite-rich one (M3), points to embrittlement then fluid ingression. Observation on preserved breccia planes of the full transition from intact metagabbro to crackle, mosaic and chaotic breccia, together with the presence of microbreccia domains and the occurrence of minerals fractured and offset along omphacite-bearing planes support the view that Monviso eclogite breccias were generated by instantaneous brittle rupture.

(4) Further strain localization into the LSZ, marked by the incorporation of unbrecciated mafic and ultramafic blocks and by network widening, was promoted by fluids and metasomatism.

Acknowledgment

This study was funded by the project "Zooming in Between Plates" (Marie Curie International Training Network of the European Union's Seventh Framework Program FP7/2007-2013/ under REA grant agreement no. 604713). We thank M. Fialin, N. Rividi (CAMPARIS), O. Boudouma (ISTeP) for analytical support, E. Delairis (ISTeP) for the preparation of thin sections and the Parco del Monviso for bureaucratical help. We also thank Tan Z., Bonnet G. and Soret M. for interesting discussions and the friends of Rifugio Alpetto for the gastronomic and moral support. Othmar Müntener and an anonymous reviewer are warmly thanked for their constructive reviews and suggestions, and Marco Scambelluri for his editorial handling leading to a significant improvement of the manuscript.

Appendix A. Supplementary data

Supplementary data to this article can be found online at https://doi.org/10.1016/j.lithos.2018.09.028.

References

Agard, P., Monié, P., Jolivet, L., Goffé, B., 2002. Exhumation of the Schistes Lustrés complex: in situ laser probe 40Ar/39Ar constraints and implications for the Western Alps. J. Metamorph. Geol. 20, 599–618.

Agard, P., Yamato, P., Jolivet, L., Burov, E., 2009. Exhumation of oceanic blueschists and eclogites in subduction zones: timing and mechanisms. Earth-Sci. Rev. 92, 53–79. https://doi.org/10.1016/j.earscirev.2008.11.002.

Angiboust, S., Agard, P., 2010. Initial water budget: the key to detaching large volumes of eclogitized oceanic crust along the subduction channel? Lithos 120, 453–474. https://doi.org/10.1016/j.lithos.2010.09.007.

Angiboust, S., Agard, P., Raimbourg, H., Yamato, P., Huet, B., 2011. Subduction interface processes recorded by eclogite-facies shear zones (Monviso, W. Alps). Lithos 127, 222–238. https://doi.org/10.1016/j.lithos.2011.09.004.

Angiboust, S., Agard, P., Yamato, P., Raimbourg, H., 2012a. Eclogite breccias in a subducted ophiolite: a record of intermediate-depth earthquakes? Geology 40, 707–710. https://doi.org/10.1130/G32925.1.

Angiboust, S., Langdon, R., Agard, P., Waters, D., Chopin, C., 2012b. Eclogitization of the Monviso ophiolite (W. Alps) and implications on subduction dynamics: MONVISO ECLOGITES AND SUBDUCTION DYNAMICS. J. Metamorph. Geol. 30, 37–61. https://doi.org/10.1111/j.1525-1314.2011.00951.x.

Angiboust, S., Pettke, T., Hoog, J.C.M.D., Caron, B., Oncken, O., 2014. Channelized Fluid Flow and Eclogite-facies Metasomatism along the Subduction Shear Zone. J. Petrol. 55, 883–916. https://doi.org/10.1093/petrology/egu010.

Austrheim, H., Boundy, T.M., 1994. Pseudotachylytes Generated during seismic faulting and eclogitization of the deep crust. Science 265, 82. https://doi.org/10.1126/science.265.5168.82.

Bachmann, R., Oncken, O., Glodny, J., Seifert, W., Georgieva, V., Sudo, M., 2009. Exposed plate interface in the European Alps reveals fabric styles and gradients related to an ancient seismogenic coupling zone. J. Geophys. Res. Solid Earth 114, B05402. https://doi.org/10.1029/2008JB005927.

Balestro, G., Fioraso, G., Lombardo, B., 2013. Geological map of the Monviso massif (Western Alps). Journal of Maps 9, 623–634. https://doi.org/10.1080/17445647.2013.842507.

Balestro, G., Lombardo, B., Vaggelli, G., Borghi, A., Festa, A., Gattiglio, M., 2014. Tectonostratigraphy of the northern Monviso Meta-ophiolite complex (Western Alps). Ital. J. Geosci. 133, 409–426. https://doi.org/10.3301/IJG.2014.13.

Balestro, G., Festa, A., Dilek, Y., Tartarotti, P., 2015a. Pre-alpine extensional tectonics of a peridotite-localized oceanic core complex in the late jurassic, High-pressure Monviso ophiolite (Western Alps). Episodes 38, 266–282.

Balestro, G., Festa, A., Tartarotti, P., 2015b. Tectonic significance of different block-in-matrix structures in exhumed convergent plate margins: examples from oceanic and continental HP rocks in Inner Western Alps (northwest Italy). Int. Geol. Rev. 57, 581–605. https://doi.org/10.1080/00206814.2014.943307.

Balestro, G., Festa, A., Borghi, A., Castelli, D., Gattiglio, M., Tartarotti, P., 2018. Role of late Jurassic intra-oceanic structural inheritance in the Alpine tectonic evolution of the Monviso meta-ophiolite complex (Western Alps). Geol. Mag. 155, 233–249. https://doi.org/10.1017/S0016756817000553.

Ballevre, M., Lagabrielle, Y., Merle, O., 1990. Tertiary ductile normal faulting as a consequence of lithospheric stacking in the western Alps. Mém. Société Géologique Fr. 156, 227–236.

Beltrando, M., Rubatto, D., Manatschal, G., 2010. From passive margins to orogens: the link between ocean-continent transition zones and (ultra) high-pressure metamorphism. Geology 38, 559–562.

Blake, M.C., Jayko, A.S., 1990. Uplift of very high pressure rocks in the western Alps : evidence for structural attenuation along low-angle faults. Mémoires de La Société Géologique de France. Presented at the Deep Structure of the Alps. Conference. Société géologique de France, pp. 237–246.

Bostock, M.G., Hyndman, R.D., Rondenay, S., Peacock, S.M., 2002. An inverted continental Moho and serpentinization of the forearc mantle. Nature 417, 536–538.

Bromiley, G.D., Pawley, A.R., 2003. The stability of antigorite in the systems MgO-SiO2-H2O (MSH) and MgO-Al2O3-SiO2-H2O (MASH): The effects of Al3+ substitution on high-pressure stability. American Mineralogist 88 (1), 99–108.

Carson, C.J., Powell, R., Clarke, G.L., 1999. Calculated mineral equilibria for eclogites in CaO-Na 2 O-FeO-MgO-Al 2 O 3-SiO 2-H 2 O: application to the Pouébo Terrane, Pam Peninsula, New Caledonia. J. Metamorph. Geol. 17, 9–24.

Castelli, D., Rostagno, C., Lombardo, B., 2002. JD-QTZ-bearing METAPLAGIOGRANITE from the MONVISO META-ophiolite (western Alps). Ofioliti 27, 81–90. https://doi.org/10.4454/ofioliti.v27i2.178.

Castelli, D., Rolfo, F., Groppo, C., Compagnoni, R., 2007. Impure marbles from the UHP Brossasco-Isasca Unit (Dora-Maira Massif, western Alps): evidence for Alpine equilibration in the diamond stability field and evaluation of the X(CO2) fluid evolution. J. Metamorph. Geol. 25, 587–603. https://doi.org/10.1111/j.1525-1314.2007.00716.x.

Cheng, H., Nakamura, E., Kobayashi, K., Zhou, Z., 2007. Origin of atoll garnets in eclogites and implications for the redistribution of trace elements during slab exhumation in a continental subduction zone. Am. Mineral. 92, 1119–1129. https://doi.org/10.2138/am.2007.2343.

Chopin, C., 1984. Coesite and pure pyrope in high-grade blueschists of the Western Alps: a first record and some consequences. Contrib. Mineral. Petrol. 86, 107–118. https://doi.org/10.1007/BF00381838.

Chopin, C., 2003. Ultrahigh-pressure metamorphism: tracing continental crust into the mantle. Earth Planet. Sci. Lett. 212, 1–14. https://doi.org/10.1016/S0012-821X(03)00261-9.

Compagnoni, R., Rolfo, F., Castelli, D., 2012. Jadeitite from the Monviso meta-ophiolite, western Alps: occurrence and genesis. Eur. J. Mineral. 24, 333–343. https://doi.org/10.1127/0935-1221/2011/0023-2164.

Connolly, J.A.D., 1990. Multivariable phase diagrams; an algorithm based on generalized thermodynamics. Am. J. Sci. 290, 666–718. https://doi.org/10.2475/ajs.290.6.666.

Connolly, J.A.D., 2005. Computation of phase equilibria by linear programming: a tool for geodynamic modeling and its application to subduction zone decarbonation. Earth Planet. Sci. Lett. 236, 524–541. https://doi.org/10.1016/j.epsl.2005.04.033.

Coward, M., Dietrich, D., 1989. Alpine tectonics — an overview. Geol. Soc. Lond. Spec. Publ. 45, 1–29. https://doi.org/10.1144/GSL.SP.1989.045.01.01.

Dal Piaz, G.V., Bistacchi, A., Massironi, M., 2003. Geological outline of the Alps. Episodes 26, 175–180.

Davies, J.H., 1999. The role of hydraulic fractures and intermediate-depth earthquakes in generating subduction-zone magmatism. Nature 398, 142–145. https://doi.org/10.1038/18202.

Deseta, N., Ashwal, L.D., Andersen, T.B., 2014. Initiating intermediate-depth earthquakes: Insights from a HP–LT ophiolite from Corsica. Lithos 206, 127–146. https://doi.org/10.1016/j.lithos.2014.07.022.

Desmurs, L., Manatschal, G., Bernoulli, D., 2001. The Steinmann Trinity revisited: mantle exhumation and magmatism along an ocean-continent transition: the Platta nappe, eastern Switzerland. Geol. Soc. Lond. Spec. Publ. 187, 235–266.

Dick, H.J.B., Tivey, M.A., Tucholke, B.E., 2008. PLutonic foundation of a slow-spreading ridge segment: Oceanic core complex at Kane Megamullion, 23 30'N, 45 20' W. Geochem. Geophys. Geosyst. 9. https://doi.org/10.1029/2007GC001645.

Diener, J.F.A., Powell, R., White, R.W., Holland, T.J.B., 2007. A new thermodynamic model for clino- and orthoamphiboles in the system Na 2 O?CaO?FeO?MgO?Al 2 O 3 ?SiO 2 ?H 2 O?O. J. Metamorph. Geol. 25, 631–656. https://doi.org/10.1111/j.1525-1314.2007.00720.x.

Duchêne, S., Blichert-Toft, J., Luais, B., Télouk, P., Lardeaux, J.M., Albarède, F., et al., 1997. The Lu-Hf dating of garnets and the ages of the Alpine high-pressure metamorphism. Nature 387, 586–588.

Escartín, J., Cannat, M., Pouliquen, G., Rabain, A., Lin, J., 2001. Crustal thickness of V-shaped ridges south of the Azores: Interaction of the Mid-Atlantic Ridge (36°–39°N) and the Azores hot spot. J. Geophys. Res. Solid Earth 106, 21719–21735. https://doi.org/10.1029/2001JB000224.

Escartín, J., Mével, C., MacLeod, C.J., McCaig, A.M., 2003. Constraints on deformation conditions and the origin of oceanic detachments: the Mid-Atlantic Ridge core complex at 15°45′N. Geochem. Geophys. Geosyst. 4, 1067. https://doi.org/10.1029/2002GC000472.

Evans, T.P., 2004. A method for calculating effective bulk composition modification due to crystal fractionation in GARNET-bearing schist: implications for isopleth thermobarometry: GARNET FRACTIONATION AND P-T PATH CALCULATION. J. Metamorph. Geol. 22, 547–557. https://doi.org/10.1111/j.1525-1314.2004.00532.x.

Festa, A., Balestro, G., Dilek, Y., Tartarotti, P., 2015. A Jurassic oceanic core complex in the high-pressure Monviso ophiolite (western Alps, NW Italy). Lithosphere 7, 646–652. https://doi.org/10.1130/L458.1.

Fuhram, M.L., Linsley, D.H., 1988. Ternary-feldspar modeling and thermometry. Am. Mineral. 73, 201–215.

Gebauer, D., Schertl, H.-P., Brix, M., Schreyer, W., 1997. 35 Ma old ultrahigh-pressure metamorphism and evidence for very rapid exhumation in the Dora Maira Massif, Western Alps. Lithos 41, 5–24. https://doi.org/10.1016/S0024-4937(97)82002-6.

Green, H.W., Houston, H., 1995. The mechanism of deep earthquacke. Annu. Rev. Earth Planet. Sci. 23, 169–214.

Green, E., Holland, T., Powell, R., 2007. An order-disorder model for omphacitic pyroxenes in the system jadeite-diopside-hedenbergite-acmite, with applications to eclogitic rocks. Am. Mineral. 92, 1181–1189. https://doi.org/10.2138/am.2007.2401.

Groppo, C., Castelli, D., 2010. Prograde P-T Evolution of a Lawsonite Eclogite from the Monviso Meta-ophiolite (Western Alps): Dehydration and Redox Reactions during Subduction of Oceanic FeTi-oxide Gabbro. J. Petrol. 51, 2489–2514. https://doi.org/10.1093/petrology/egq065.

Hacker, B.R., Abers, G.A., Peacock, S.M., 2003a. Subduction factory 1. Theoretical mineralogy, densities, seismic wave speeds, and H_2O contents: SUBDUCTION ZONE MINERALOGY AND PHYSICAL PROPERTIES. J. Geophys. Res. Solid Earth 108. https://doi.org/10.1029/2001JB001127.

Hacker, B.R., Peacock, S.M., Abers, G.A., Holloway, S.D., 2003b. Subduction factory 2. Are intermediate-depth earthquakes in subducting slabs linked to metamorphic dehydration reactions?: SUBDUCTION ZONE EARTHQUAKES AND DEHYDRATION. J. Geophys. Res. Solid Earth 108. https://doi.org/10.1029/2001JB001129.

Hilairet, N., Reynard, B., Wang, Y., Daniel, I., Merkel, S., Nishiyama, N., Petitgirard, S., 2007. High-pressure creep of serpentine, interseismic deformation, and initiation of subduction. Science 318, 1910–1913. https://doi.org/10.1126/science.1148494.

Holland, T., Powell, R., 1991. A compensated-Redlich-Kwong (CORK) equation for volumes and fugacities of CO_2 and H_2O in the range 1 bar to 50 kbar and 100–1600 C. Contrib. Mineral. Petrol. 109, 265–273.

Holland, T.J.B., Powell, R., 1998. An internally consistent thermodynamic data set for phases of petrological interest. J. Metamorph. Geol. 16, 309–343.

Holland, T., Powell, R., 2003. Activity? Composition relations for phases in petrological calculations: an asymmetric multicomponent formulation. Contrib. Mineral. Petrol. 145, 492–501. https://doi.org/10.1007/s00410-003-0464-z.

Ikesawa, E., Sakaguchi, A., Kimura, G., 2003. Pseudotachylyte from an ancient accretionary complex: evidence for melt generation during seismic slip along a master décollement? Geology 31, 637–640. https://doi.org/10.1130/0091-7613(2003)031<0637:PFAAAC>2.0.CO;2.

Jébrak, M., 1997. Hydrothermal breccias in vein-type ore deposits: a review of mechanisms, morphology and size distribution. Ore Geol. Rev. 12, 111–134. https://doi.org/10.1016/S0169-1368(97)00009-7.

Jin, Z.-M., Zhang, J., Green, H.W., Jin, S., 2001. Eclogite rheology: Implications for subducted lithosphere. Geology 29, 667–670. https://doi.org/10.1130/0091-7613(2001)029<0667:ERIFSL>2.0.CO;2.

John, T., Medvedev, S., Rüpke, L.H., Andersen, T.B., Podladchikov, Y.Y., Austrheim, H., 2009. Generation of intermediate-depth earthquakes by self-localizing thermal runaway. Nat. Geosci. 2, 137–140. https://doi.org/10.1038/ngeo419.

Jung, H., Green, H.W., 2004. Experimental faulting of serpentinite during dehydration: implications for earthquakes, seismic low-velocity zones, and anomalous hypocenter distributions in subduction zones. Int. Geol. Rev. 46, 1089–1102. https://doi.org/10.2747/0020-6814.46.12.1089.

Jung, H., Green Ii, H.W., Dobrzhinetskaya, L.F., 2004. Intermediate-depth earthquake faulting by dehydration embrittlement with negative volume change. Nature 428, 545–549. https://doi.org/10.1038/nature02412.

Kirby, S.H., Kronenberg, A.K., 1984. Deformation of clinopyroxenite: evidence for a transition in flow mechanisms and semibrittle behavior. J. Geophys. Res. Solid Earth 89, 3177–3192. https://doi.org/10.1029/JB089iB05p03177.

Kirby, S., Engdahl, R., Denlinger, R., 1996. Intermediate-depth intraslab earthquakes and arc volcanism as physical expressions of crustal and uppermost mantle metamorphism in subducting slabs. Subduction Top Bottom 195–214.

Kuge, K., Kase, Y., Urata, Y., Campos, J., Perez, A., 2010. Rupture characteristics of the 2005 Tarapaca, northern Chile, intermediate-depth earthquake: evidence for heterogeneous fluid distribution across the subducting oceanic plate? J. Geophys. Res. 115. https://doi.org/10.1029/2009JB007106.

Lagabrielle, Y., Cannat, M., 1990. Alpine Jurassic ophiolites resemble the modern Central Atlantic basement. Geology 18, 319–322. https://doi.org/10.1130/0091-7613(1990)018<0319:AJORTM>2.3.CO;2.

Lagabrielle, Y., Lemoine, M., 1997. Alpine, Corsican and Apennine ophiolites: the slow-spreading ridge model. Comptes Rendus Académie Sci. - Ser. IIA - Earth Planet. Sci. 325, 909–920. https://doi.org/10.1016/S1251-8050(97)82369-5.

Lagabrielle, Y., 2009. Mantle exhumation and lithospheric spreading: An historical perspective from investigations in the Oceans and in the Alps-Apennines ophiolites. Bollettino della Societa Geologica Italiana 128 (2), 279–293.

Lagabrielle, Y., Vitale Brovarone, A., Ildefonse, B., 2015. Fossil oceanic core complexes recognized in the blueschist metaophiolites of Western Alps and Corsica. Earth-Sci. Rev. 141, 1–26. https://doi.org/10.1016/j.earscirev.2014.11.004.

Laubscher, H., 1991. The arc of the Western Alps today. Eclogae Geol. Helv. 84, 359–631.

Lifishin, E., Gauvin, R., 2001. Minimizing errors in electron microprobe analysis. Micro. Microanal. Microsc. Microanal. 7, 168–177. https://doi.org/10.1007/S100050010084.

Lissenberg, C.J., Rioux, M., Shimizu, N., Bowring, S.A., Mével, C., 2009. Zircon Dating of Oceanic Crustal Accretion. Science 323, 1048–1050. https://doi.org/10.1126/science.1167330.

Lombardo, B., 1978. Osservazioni preliminari sulle ofioliti metamorfiche del Monviso (Alpi Occidentali). Rendiconti Della Soc. Ital. Mineral. E Petrol. 34, 235–305.

Lombardo, B., Rubatto, D., Castelli, D., 2002. Ion microprobe U-PB dating of zircon from a Monviso metaplagiogranite: Implications for the evolution of the Piedmont-Liguria tethys in the Western Alps. Ofioliti 27, 109–117.

Magott, R., Fabbri, O., Fournier, M., 2016. Subduction zone intermediate-depth seismicity: Insights from the structural analysis of Alpine high-pressure ophiolite-hosted pseudotachylyte (Corsica, France). J. Struct. Geol. 87, 95–114. https://doi.org/10.1016/j.jsg.2016.04.002.

Malusà, M.G., Faccenna, C., Garzanti, E., Polino, R., 2011. Divergence in subduction zones and exhumation of high pressure rocks (Eocene Western Alps). Earth Planet. Sci. Lett. 310, 21–32. https://doi.org/10.1016/j.epsl.2011.08.002.

Manatschal, G., Müntener, O., 2009. A type sequence across an ancient magma-poor ocean–continent transition: the example of the western Alpine Tethys ophiolites. Tectonophysics 473, 4–19. https://doi.org/10.1016/j.tecto.2008.07.021.

Marroni, M., Pandolfi, L., 2007. The architecture of an incipient oceanic basin: a tentative reconstruction of the Jurassic Liguria-Piemonte basin along the Northern Apennines–Alpine Corsica transect. Int. J. Earth Sci. 96, 1059–1078. https://doi.org/10.1007/s00531-006-0163-x.

Marthaler, M., Stampfli, G.M., 1989. Les Schistes lustrés à ophiolites de la nappe du Tsaté: un ancien prisme d'accrétion issu de la marge active apulienne? Schweiz. Mineral. Petrogr. Mitt. 69, 211–216.

Means, W.D., 1995. Shear zones and rock history. Tectonophysics, 30 Years of Tectonophysics a Special Volume in Honour of Gerhard Oertel. 247, pp. 157–160. https://doi.org/10.1016/0040-1951(95)98214-H.

Meneghini, F., Toro, G.D., Rowe, C.D., Moore, J.C., Tsutsumi, A., Yamaguchi, A., 2010. Record of mega-earthquakes in subduction thrusts: the black fault rocks of Pasagshak Point (Kodiak Island, Alaska). Geol. Soc. Am. Bull. 122, 1280–1297. https://doi.org/10.1130/B30049.1.

Messiga, Kienast, Rebay, Riccardi, Tribuzio, 1999. Cr-rich magnesiochloritoid eclogites from the Monviso ophiolites (Western Alps, Italy). J. Metamorph. Geol. 17, 287–299. https://doi.org/10.1046/j.1525-1314.1999.00198.x.

Mort, K., Woodcock, N.H., 2008. Quantifying fault breccia geometry: Dent Fault, NW England. J. Struct. Geol. 30, 701–709. https://doi.org/10.1016/j.jsg.2008.02.005.

Nakajima, J., Tsuji, Y., Hasegawa, A., Kita, S., Okada, T., Matsuzawa, T., 2009. Tomographic imaging of hydrated crust and mantle in the subducting Pacific slab beneath Hokkaido, Japan: Evidence for dehydration embrittlement as a cause of intraslab earthquakes. Gondwana Res. 16, 470–481. https://doi.org/10.1016/j.gr.2008.12.010.

Padrón-Navarta, J.A., Hermann, J., Garrido, C.J., Sánchez-Vizcaíno, V.L., Gómez-Pugnaire, M.T., 2010. An experimental investigation of antigorite dehydration in natural silica-enriched serpentinite. Contributions to Mineralogy and Petrology 159 (1), 25.

Pawley, A.R., 1994. The pressure and temperature stability limits of lawsonite: implications for H2O recycling in subduction zones. Contrib. Mineral. Petrol. 118, 99–108.

Peacock, S.M., Wang, K., 1999. Seismic consequences of warm versus cool subduction metamorphism: Examples from southwest and northeast Japan. Science 286 (5441), 937–939.

Philippot, P., 1987. "Crack seal" vein geometry in eclogitic rocks. Geodin. Acta 1, 171–181. https://doi.org/10.1080/09853111.1987.11105136.

Philippot, P., 1990. Opposite vergence of Nappes and crustal extension in the French-Italian western Alps. Tectonics 9, 1143–1164. https://doi.org/10.1029/TC009i005p01143.

Philippot, P., Kienast, J.-R., 1989. Chemical-microstructural changes in eclogite-facies shear zones (Monviso, Western Alps, north Italy) as indicators of strain history and the mechanism and scale of mass transfer. Lithos 23, 179–200. https://doi.org/10.1016/0024-4937(89)90004-2.

Philippot, P., Selverstone, J., 1991. Trace-element-rich brines in eclogitic veins: implications for fluid composition and transport during subduction. Contrib. Mineral. Petrol. 106, 417–430. https://doi.org/10.1007/BF00321985.

Philippot, P., van Roermund, H.L.M., 1992. Deformation processes in eclogitic rocks: evidence for the rheological delamination of the oceanic crust in deeper levels of subduction zones. J. Struct. Geol., Mech. Instab. Rocks Tect. 14, 1059–1077. https://doi.org/10.1016/0191-8141(92)90036-V.

Plunder, A., Agard, P., Chopin, C., Okay, A.I., 2013. Geodynamics of the Tavşanlı zone, western Turkey: Insights into subduction/obduction processes. Tectonophysics 608, 884–903. https://doi.org/10.1016/j.tecto.2013.07.028.

Pognante, U., Kienast, J.-R., 1987. Blueschist and Eclogite transformations in Fe-Ti Gabbros: a Case from the Western Alps Ophiolites. J. Petrol. 28, 271–292. https://doi.org/10.1093/petrology/28.2.271.

Preston, L.A., Creager, K.C., Crosson, R.S., Brocher, T.M., Trehu, A.M., 2003. Intraslab Earthquakes: Dehydration of the Cascadia Slab. Science 302, 1197–1200. https://doi.org/10.1126/science.1090751.

Raleigh, C.B., 1967. Tectonic implications of serpentinite weakening. Geophys. J. Int. 14, 113–118. https://doi.org/10.1111/j.1365-246X.1967.tb06229.x.

Raleigh, C.B., Paterson, M.S., 1965. Experimental deformation of serpentinite and its tectonic implications. J. Geophys. Res. 70, 3965–3985. https://doi.org/10.1029/JZ070i016p03965.

Rondenay, S., Abers, G.A., van Keken, P.E., 2008. Seismic imaging of subduction zone metamorphism. Geology 36, 275. https://doi.org/10.1130/G24112A.1.

Rowe, C.D., Moore, J.C., Meneghini, F., McKeirnan, A.W., 2005. Large-scale pseudotachylytes and fluidized cataclasites from an ancient subduction thrust fault. Geology 33, 937–940. https://doi.org/10.1130/G21856.1.

Rubatto, D., Angiboust, S., 2015. Oxygen isotope record of oceanic and high-pressure metasomatism: a P–T–time–fluid path for the Monviso eclogites (Italy). Contrib. Mineral. Petrol. 170, 1–16. https://doi.org/10.1007/s00410-015-1198-4.

Rubatto, D., Hermann, J., 2003. Zircon formation during fluid circulation in eclogites (Monviso, Western Alps): implications for Zr and Hf budget in subduction zones. Geochim. Cosmochim. Acta 67, 2173–2187. https://doi.org/10.1016/S0016-7037(02)01321-2.

Rueden, C.T., Schindelin, J., Hiner, M.C., DeZonia, B.E., Walter, A.E., Arena, E.T., Eliceiri, K.W., 2017. ImageJ2: ImageJ for the next generation of scientific image data. BMC Bioinformatics 18. https://doi.org/10.1186/s12859-017-1934-z.

Rutter, E.H., 1986. On the nomenclature of mode of failure transitions in rocks. Tectonophysics 122, 381–387. https://doi.org/10.1016/0040-1951(86)90153-8.

Scambelluri, M., Strating, E.H.H., Piccardo, G.B., Vissers, R.L.M., Rampone, E., 1991. Alpine olivine- and titanian clinohumite-bearing assemblages in the Erro-Tobbio peridotite (Voltri Massif, NW Italy). J. Metamorph. Geol. 9, 79–91. https://doi.org/10.1111/j.1525-1314.1991.tb00505.x.

Scambelluri, M., Pennacchioni, G., Gilio, M., Bestmann, M., Plümper, O., Nestola, F., 2017. Fossil intermediate-depth earthquakes in subducting slabs linked to differential stress release. Nat. Geosci. 10, 960–966. https://doi.org/10.1038/s41561-017-0010-7.

Schertl, H.-P., Schreyer, W., Chopin, C., 1991. The pyrope-coesite rocks and their country rocks at Parigi, Dora Maira Massif, Western Alps: detailed petrography, mineral chemistry and PT-path. Contrib. Mineral. Petrol. 108, 1–21. https://doi.org/10.1007/BF00307322.

Schindelin, J., Arganda-Carreras, I., Frise, E., Kaynig, V., Longair, M., Pietzsch, T., Preibisch, S., Rueden, C., Saalfeld, S., Schmid, B., Tinevez, J.-Y., White, D.J., Hartenstein, V., Eliceiri, K., Tomancak, P., Cardona, A., 2012. Fiji: an open-source platform for biological-image analysis. Nat. Methods 9, 676–682. https://doi.org/10.1038/nmeth.2019.

Schmid, S.M., Kissling, E., 2000. The arc of the western Alps in the light of geophysical data on deep crustal structure. Tectonics 19, 62–85. https://doi.org/10.1029/1999TC900057.

Schmid, S.M., Fügenschuh, B., Kissling, E., Schuster, R., 2004. Tectonic map and overall architecture of the Alpine orogen. Eclogae Geol. Helv. 97, 93–117. https://doi.org/10.1007/s00015-004-1113-x.

Schüler, T., Manke, R., Jänicke, R., Radenberg, M., Steeb, H., 2013. Multi-scale modelling of elastic/viscoelastic compounds. ZAMM - J. Appl. Math. Mech. Z. Für Angew. Math. Mech. 93, 126–137. https://doi.org/10.1002/zamm.201200055.

Schwartz, S., Lardeaux, J.-M., Guillot, S., Tricart, P., 2000. Diversité du métamorphisme éclogitique dans le massif ophiolitique du Monviso (Alpes occidentales, Italie). Geodin. Acta 13, 169–188. https://doi.org/10.1080/09853111.2000.11105371.

Shiina, T., Nakajima, J., Matsuzawa, T., 2013. Seismic evidence for high pore pressures in the oceanic crust: Implications for fluid-related embrittlement. Geophys. Res. Lett. 40, 2006–2010. https://doi.org/10.1002/grl.50468.

Sibson, R.H., 1986. Brecciation processes in fault zones: Inferences from earthquake rupturing. Pure Appl. Geophys. 124, 159–175. https://doi.org/10.1007/BF00875724.

Spandler, C., Pettke, T., Rubatto, D., 2011. Internal and External Fluid sources for Eclogite-facies Veins in the Monviso Meta-ophiolite, Western Alps: Implications for Fluid Flow in Subduction zones. J. Petrol. 52, 1207–1236. https://doi.org/10.1093/petrology/egr025.

Strömgård, K.-E., 1973. Stress distribution during formation of boudinage and pressure shadows. Tectonophysics 16, 215–248. https://doi.org/10.1016/0040-1951(73)90013-9.

Toyoshima, T., 1990. Pseudotachylite from the Main Zone of the Hidaka metamorphic belt, Hokkaido, northern Japan. J. Metamorph. Geol. 8, 507–523. https://doi.org/10.1111/j.1525-1314.1990.tb00483.x.

Treagus, S.H., 1981. A theory of stress and strain variations in viscous layers, and its geological implications. Tectonophysics 72, 75–103. https://doi.org/10.1016/0040-1951(81)90088-3.

Tsuji, Y., Nakajima, J., Hasegawa, A., 2008. Tomographic evidence for hydrated oceanic crust of the Pacific slab beneath northeastern Japan: Implications for water transportation in subduction zones. Geophys. Res. Lett. 35, L14308. https://doi.org/10.1029/2008GL034461.

Ulmer, P., Trommsdorff, V., 1995). Serpentine stability to mantle depths and subduction-related magmatism. Science 268 (5212), 858–861.

Vannucchi, P., Sage, F., Phipps Morgan, J., Remitti, F., Collot, J.-Y., 2012. Toward a dynamic concept of the subduction channel at erosive convergent margins with implications for interplate material transfer. Geochem. Geophys. Geosyst. 13, Q02003. https://doi.org/10.1029/2011GC003846.

Yamasaki, T., Seno, T., 2003. Double seismic zone and dehydration embrittlement of the subducting slab. J. Geophys. Res. Solid Earth 108, 2212. https://doi.org/10.1029/2002JB001918.

Yang, J.-J., Huang, M.-X., Wu, Q.-Y., Zhang, H.-R., 2014. Coesite-bearing eclogite breccia: implication for coseismic ultrahigh-pressure metamorphism and the rate of the process. Contrib. Mineral. Petrol. 167, 1013. https://doi.org/10.1007/s00410-014-1013-7.